nature energy

Article

https://doi.org/10.1038/s41560-024-01465-2

Suppressing strain propagation in ultrahigh-Ni cathodes during fast charging via epitaxial entropy-assisted coating

In the format provided by the authors and unedited

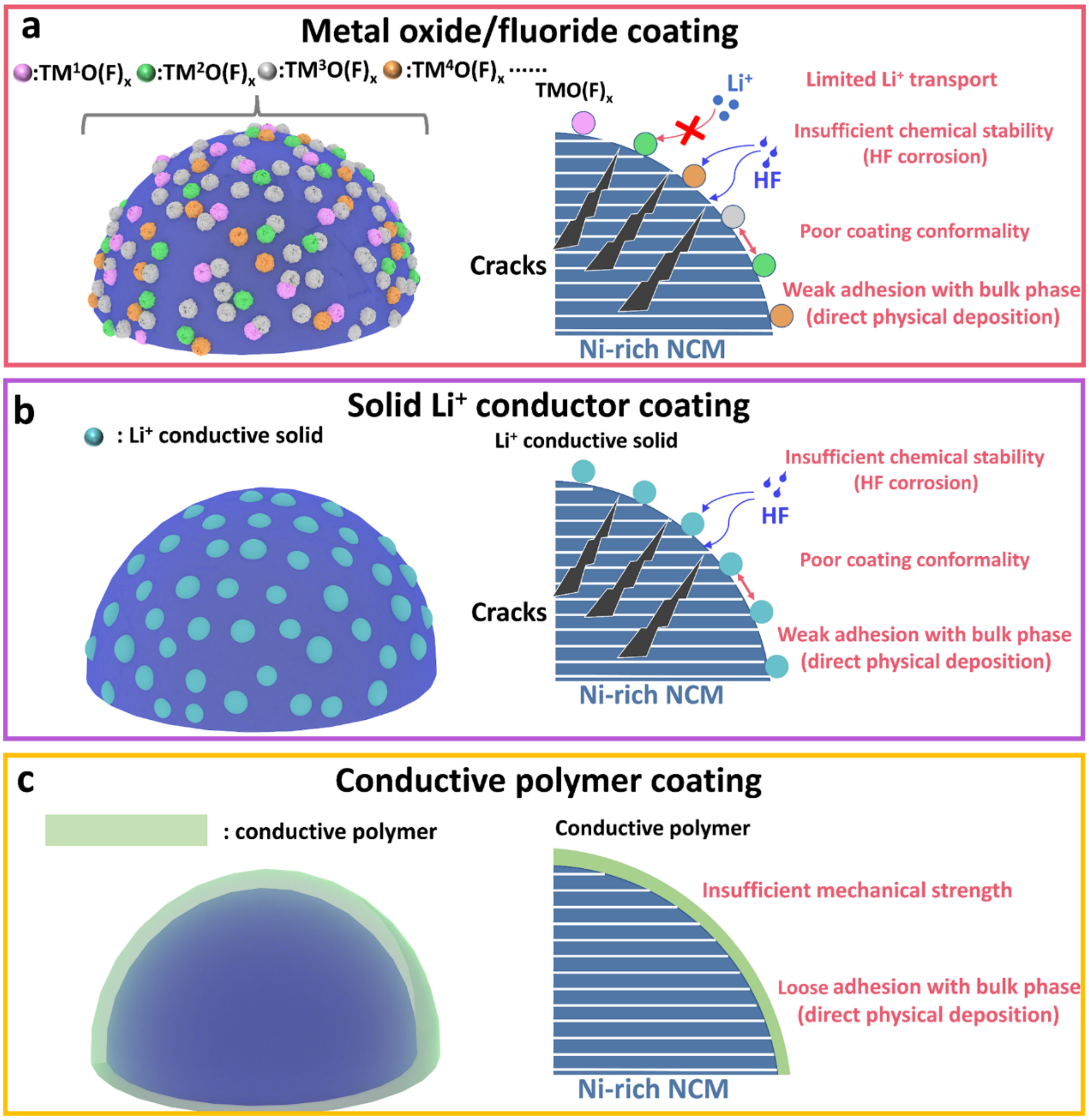

Supplementary Fig. 1 | Limitations of conventional surface coating technologies. Schematic illustrations of **a,** conventional metal oxide/fluoride coating; **b,** conventional solid Li^+ conductor coating; c, conventional conductive polymer coating.

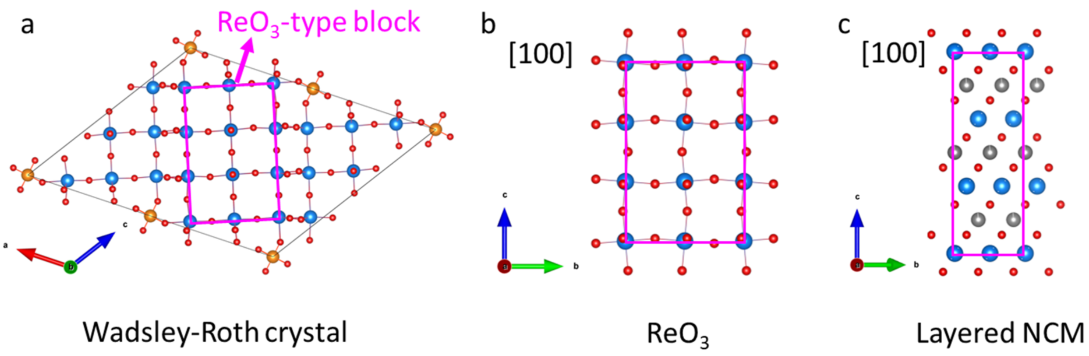

Supplementary Fig. 2 | Schematic illustration of crystal structures. a, Wadsley-Roth crystallographic shear structure. **b,** ReO_3. **c,** Layered NCM.

The Wadsley-Roth phases generally occur in the chemical systems of Nb_2O_5-NbO_2, Nb_2O_5-TiO_2, and Nb_2O_5-WO_3, and the crystal structures are built by n × m × ∞ ReO_3 type units. In this work, we used the $Nb_{12}WO_{33}$ $(3 \times 4)_{\infty}$ ReO_3-type as the proof-of-concept. As shown in Supplementary Fig. 2, the ReO_3-type block inside the $Nb_{12}WO_{33}$ exhibited parallel orientation to layered NCM in the [100] direction, which could induce the oriented-attachment-driven reaction between the surface of NCM and nano-sized precursors to epitaxially form a high-entropy oxide layer whose lattice is well aligned with the bulk layered structure.

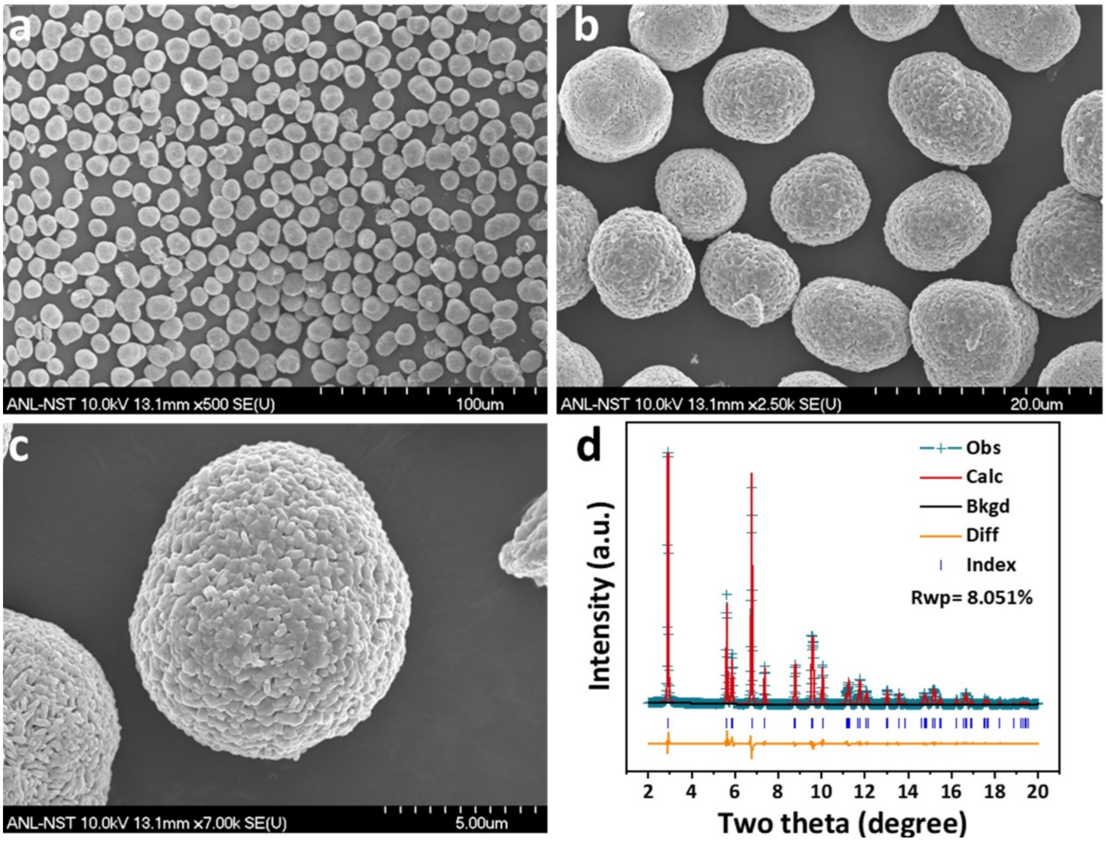

Supplementary Fig. 3 | a-c, SEM images of Ni90 powder. **d,** Synchrotron HEXRD Rietveld refinement of Ni90 powder. Wavelength is 0.24079Å.

As characterized by SEM, the synthesized Ni90 exhibited typical polycrystalline morphology with a particle size of ~ 10 µm. The HEXRD Rietveld refinement result of Ni90 exhibited a typical $R\bar{3}m$ space group with the lattice parameters: $a = b = 2.87224$ Å; $c = 14.1804$ Å.

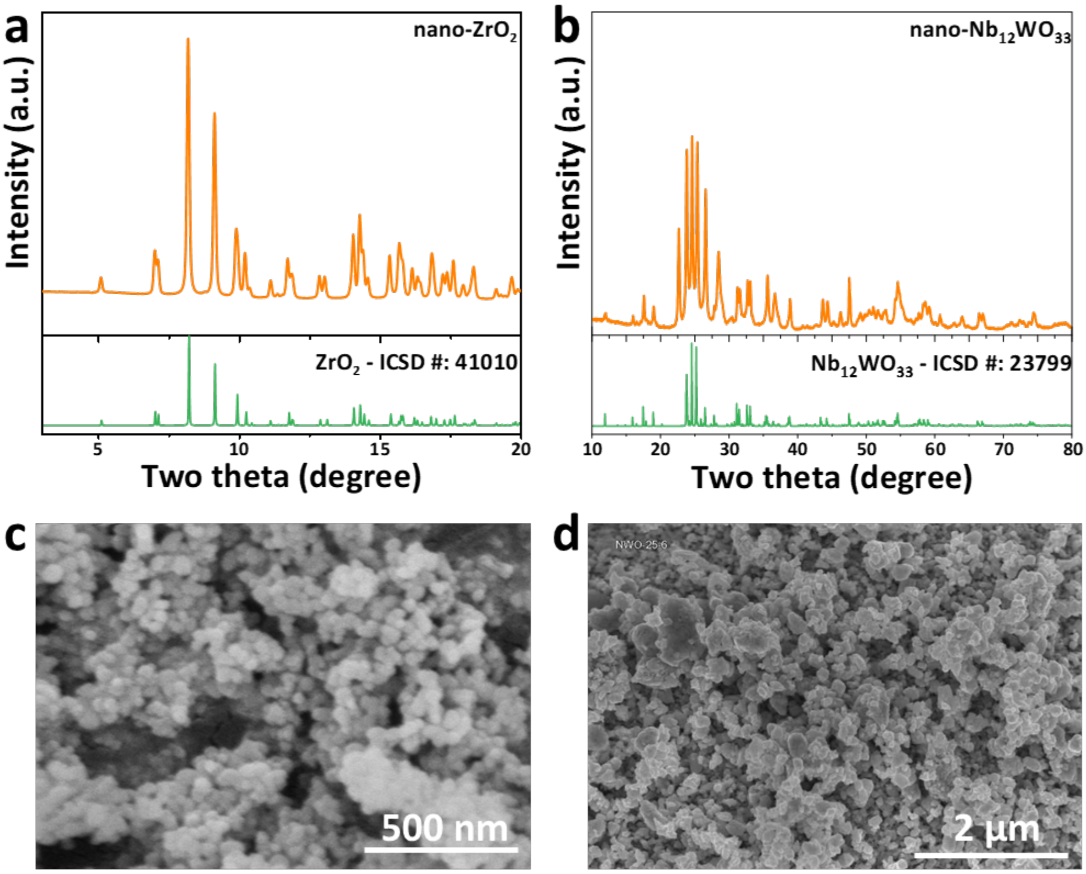

Supplementary Fig. 4 | a, HEXRD pattern of nano-sized ZrO_2 powder. **b,** HEXRD pattern of nano-sized $Nb_{12}WO_{33}$ powder. **c,** SEM image of nano-sized ZrO_2 powder. **d,** SEM image of nano-sized $Nb_{12}WO_{33}$ powder.

As shown, the HEXRD patterns of nano-sized ZrO_2 and $Nb_{12}WO_{33}$ agreed well with the standard references (ZrO_2 ICSD code: 41010; $Nb_{12}WO_{33}$ ICSD code: 23799). The particle size of nano-sized ZrO_2 was ~ 30 nm, and the particle size of nano-sized $Nb_{12}WO_{33}$ was ~ 100 nm.

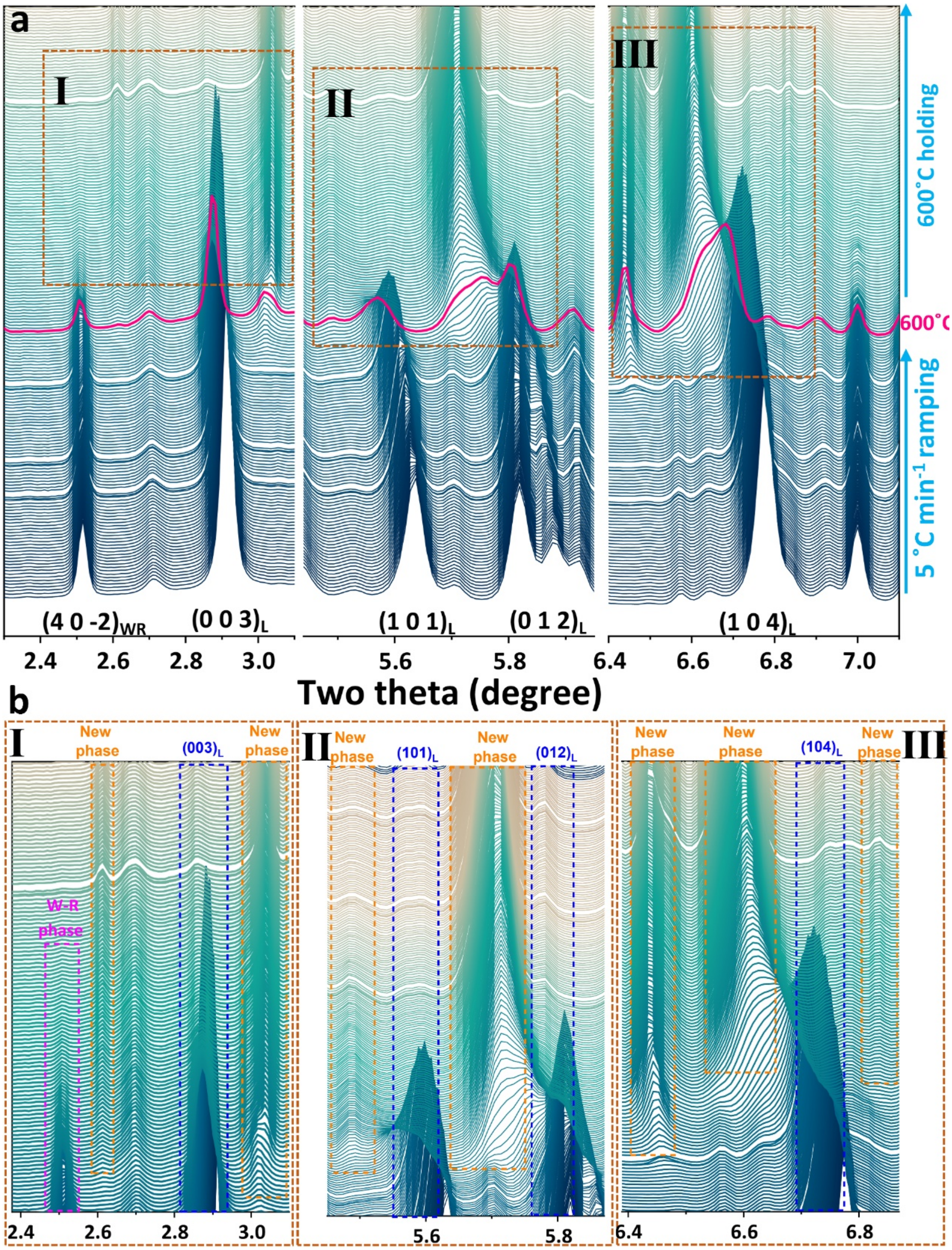

Supplementary Fig. 5 | In-situ synchrotron HEXRD patterns during formation of high-entropy oxide phases. a, The in-situ HEXRD diffraction peaks evolution during calcination process. **b,** The enlarged diffraction peaks corresponding to the selected area (I, II, and III) in Supplementary Fig. 5a.

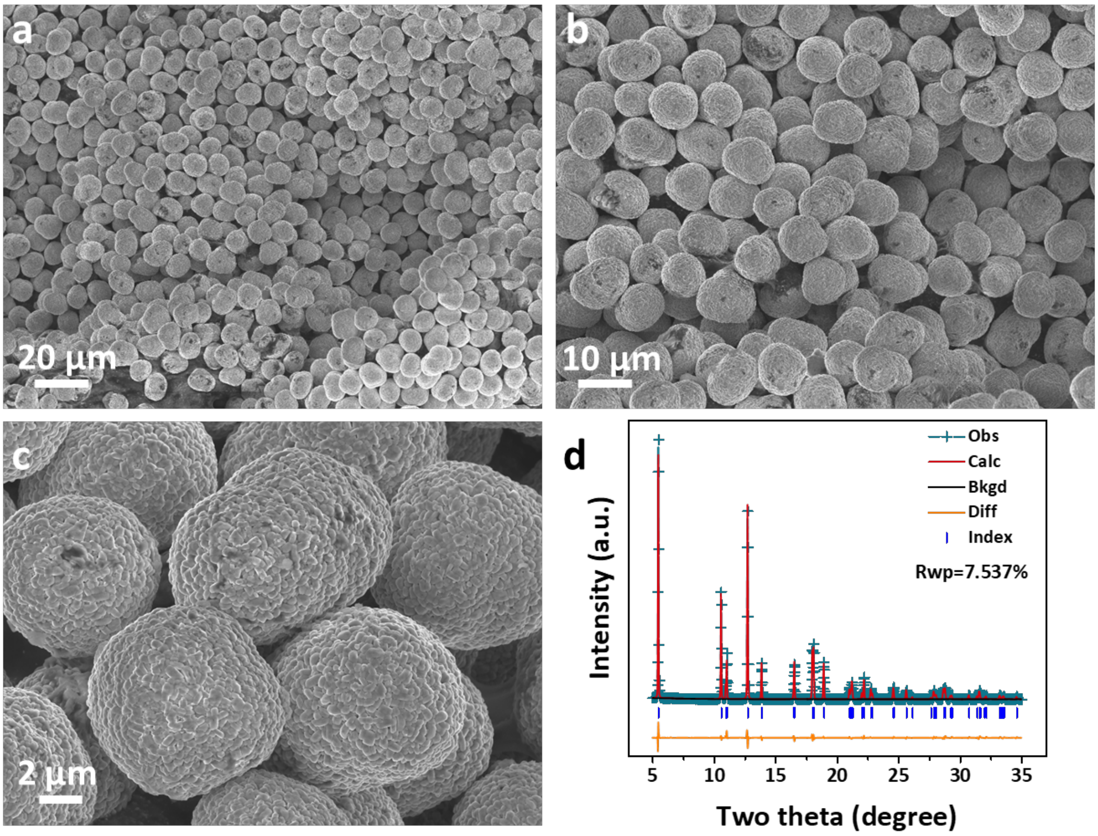

Supplementary Fig. 6 | a-c, SEM images of EEC-Ni90 powder. **d,** Synchrotron HEXRD Rietveld refinement of EEC-Ni90 powder. Wavelength is 0.45199Å.

As characterized by SEM, EEC-Ni90 exhibited a polycrystalline morphology that was similar to Ni90, and the particle size was measured to be ~ 10 µm. No agglomerates were found in the EEC-Ni90, indicating the homogeneous EEC on the surface of NCM particles. The HEXRD Rietveld refinement result of EEC-Ni90 exhibited a typical $R\bar{3}m$ space group with a slightly larger lattice parameters (a = b = 2.87455 Å; c = 14.19792 Å) than that of Ni90, which might be due to the large lattice parameter of $Nb_{12}WO_{33}$ (a = 22.37 Å, b = 3.825 Å, c = 17.87 Å).

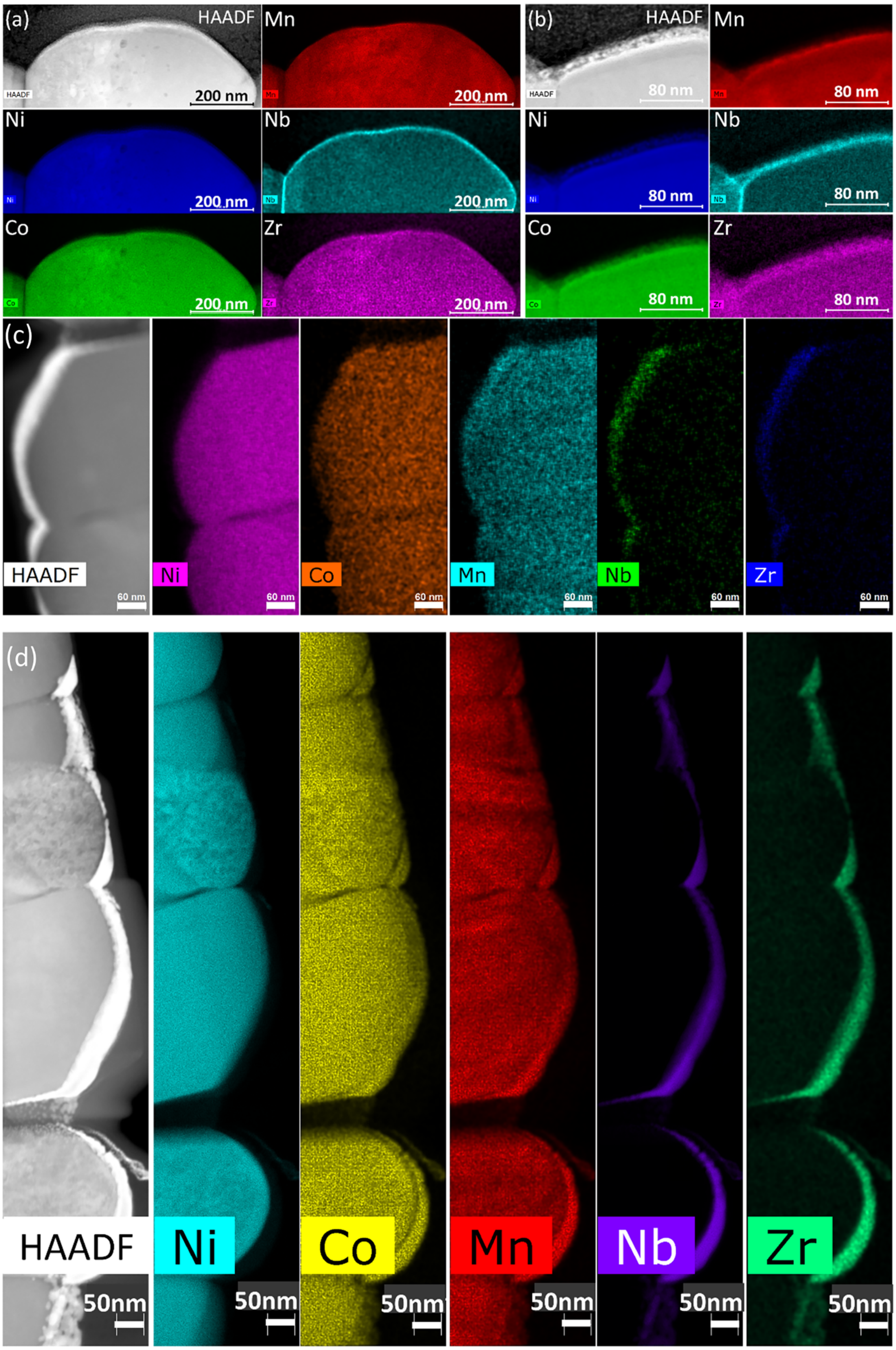

Supplementary Fig. 7 | HAADF-STEM elemental mapping of multiple EEC-Ni90 particles. Cross-section TEM images of EEC-Ni90 and the corresponding EDS element mappings. The interest-of-elements are Ni, Co, Mn, Nb, and Zr.

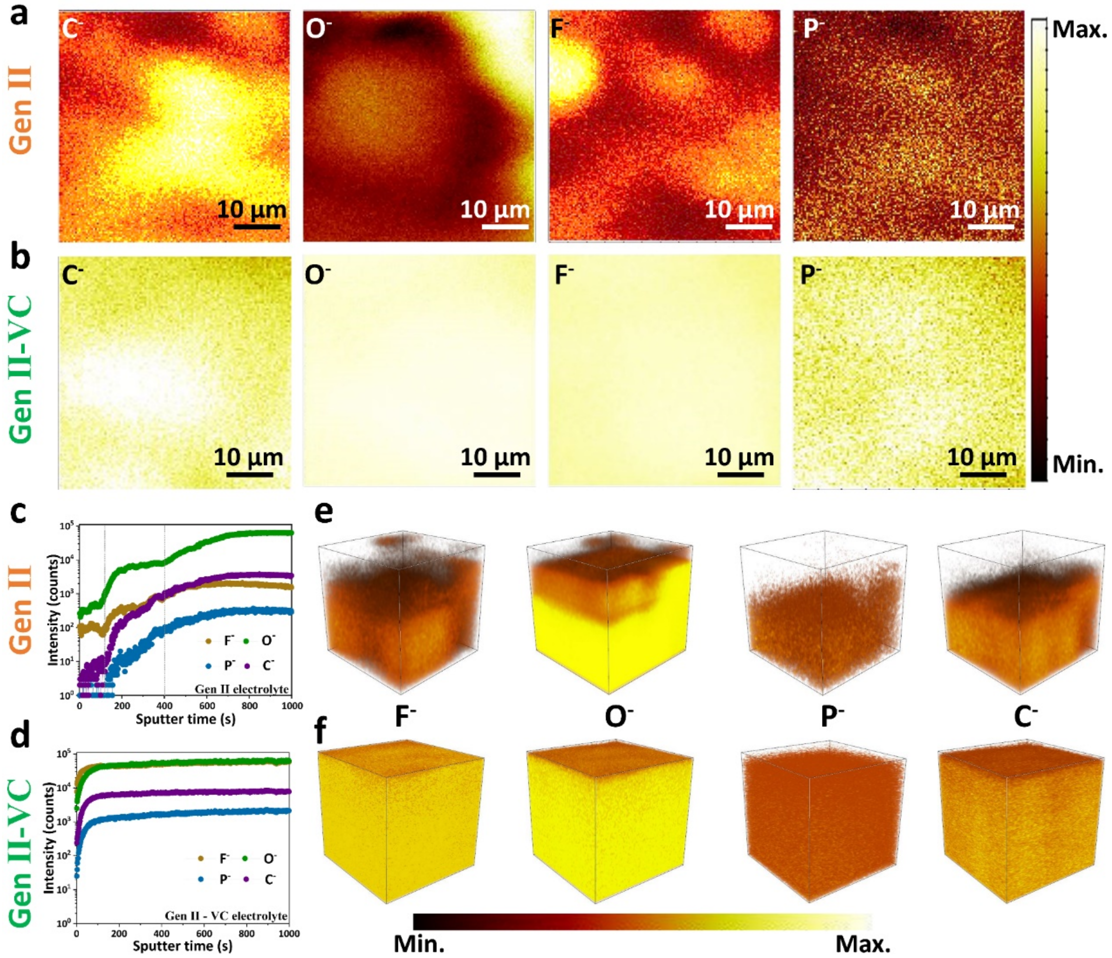

Supplementary Fig. 8 | Surface characterization of cycled Li metal anode of Li/EEC-Ni90 cells in different electrolytes. Time-of-flight secondary ion mass spectrometry (ToF-SIMS) element mappings of Li metal anode after 20 cycles in **a,** Gen II; and **b,** Gen II-VC electrolytes. ToF-SIMS element depth profiling of Li metal anode after 20 cycles in **c,** Gen II; and **d,** Gen II-VC electrolytes. ToF-SIMS element 3D reconstructions (F^-, O^-, P^-, and C^-) of Li metal anode after 20 cycles in **e,** Gen II; and **f,** Gen II-VC electrolytes.

Time-of-flight secondary ion mass spectrometry (ToF-SIMS) characterizations were carried out to analyze the surface of cycled Li metal anode of Li/EEC-Ni90 cells after 20 cycles of charge/discharge in electrolyte with and without 2 wt.%VC additive. The C^-, O^-, F^-, and P^- element distributions can be used to analyze the as-formed solid-electrolyte interface (SEI) on the cycled Li metal. In plain Gen II electrolyte, the surface exhibits non-uniform distribution features (Supplementary Fig. 8a), indicating the morphological and compositional heterogeneities of SEI. By contrast, after introducing

VC into the electrolyte, a homogeneous SEI layer (Supplementary Fig. 8b) was induced on the surface of the cycled Li metal anode.

Depth profiling ToF-SIMS investigations were further conducted. As shown in Supplementary Fig. 8c, three obvious element distribution regions can be identified on the cycled Li metal surface in Gen II electrolyte, where the intensities of elements gradually increase as the thickness deepens, suggesting the formation of highly tortuous SEI in plain Gen II electrolyte. With VC additive, all elements' intensities quickly increase and remain stable afterward (Supplementary Fig. 8d), suggesting the homogeneous SEI formation feature. The 3D element reconstructions provide direct visualization of the induced SEI in the electrolytes with and without VC additive. As shown in Supplementary Fig. 8e, without VC additive, the SEI exhibits significant heterogeneity in both vertical and horizontal directions. In the case with the VC additive, the morphological and compositional homogeneity of the SEI were greatly improved (Supplementary Fig. 8f), indicating VC can effectively regulate the interface property to stabilize the Li metal anode.

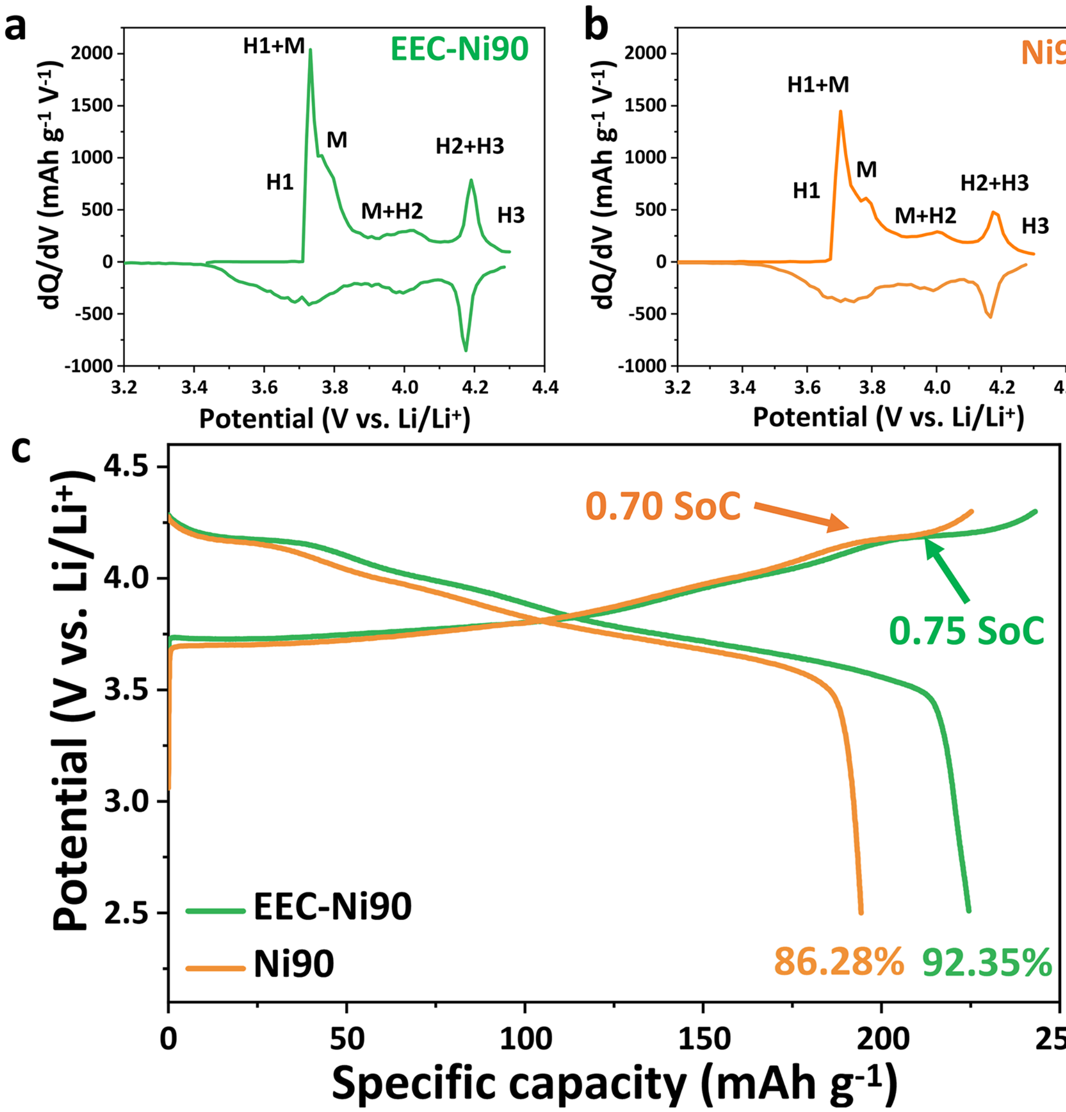

Supplementary Fig. 9 | Differential capacity (dQ/dV) profiles of **a,** EEC-Ni90; and **b,** bare Ni90 cathode at 0.1C. **c,** Charge-discharge voltage profiles of the initial cycle for Ni90 and EEC-Ni90 cathode at 0.1C.

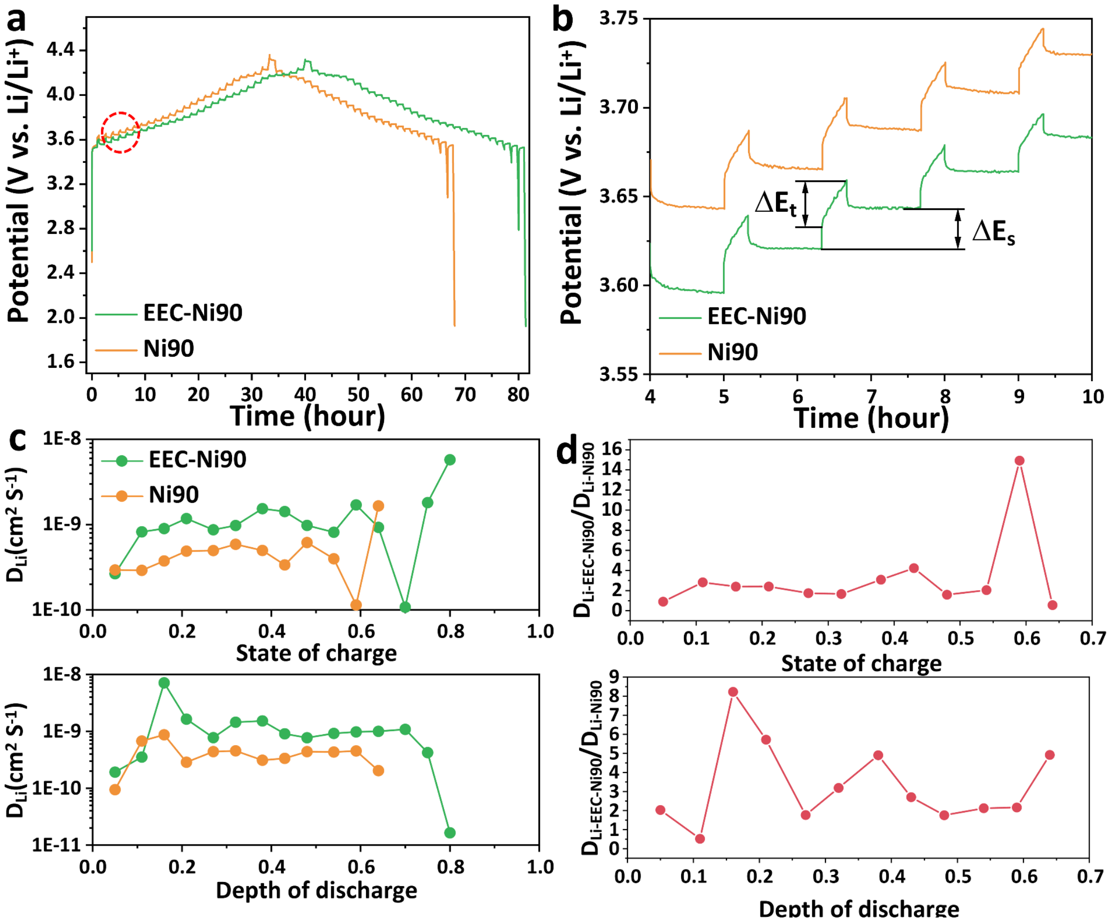

Supplementary Fig. 10 | GITT characterization. a-b, Voltage profiles of the GITT measurements for Ni90 and EEC-Ni90 cathode. **c,** Measured Li^+ diffusion coefficient during charge/discharge process. **d,** The ratio for the Li^+ diffusion coefficient of EEC-Ni90 over that of bare Ni90 cathode at the same SoC and DoD.

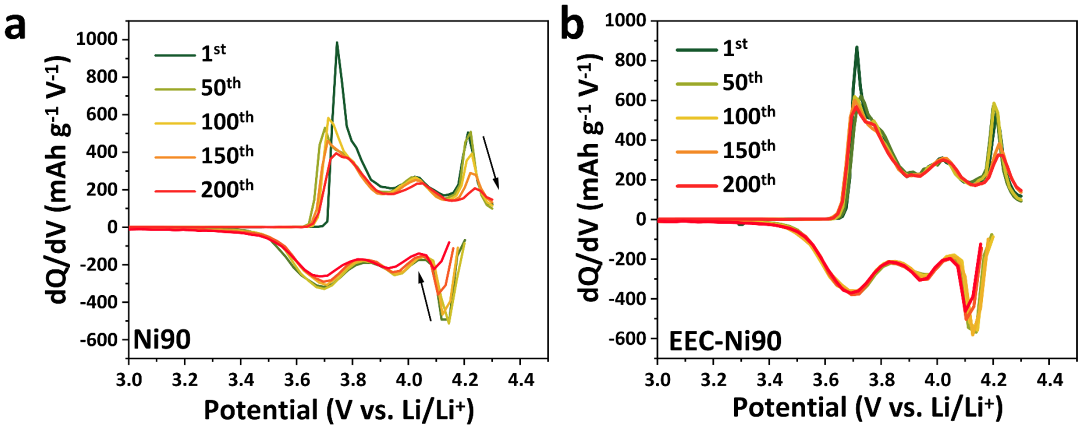

Supplementary Fig. 11 | Differential capacity (dQ/dV) curves of **a,** bare Ni90; and **b,** EEC-Ni90 cathode during charge/discharge at 1C.

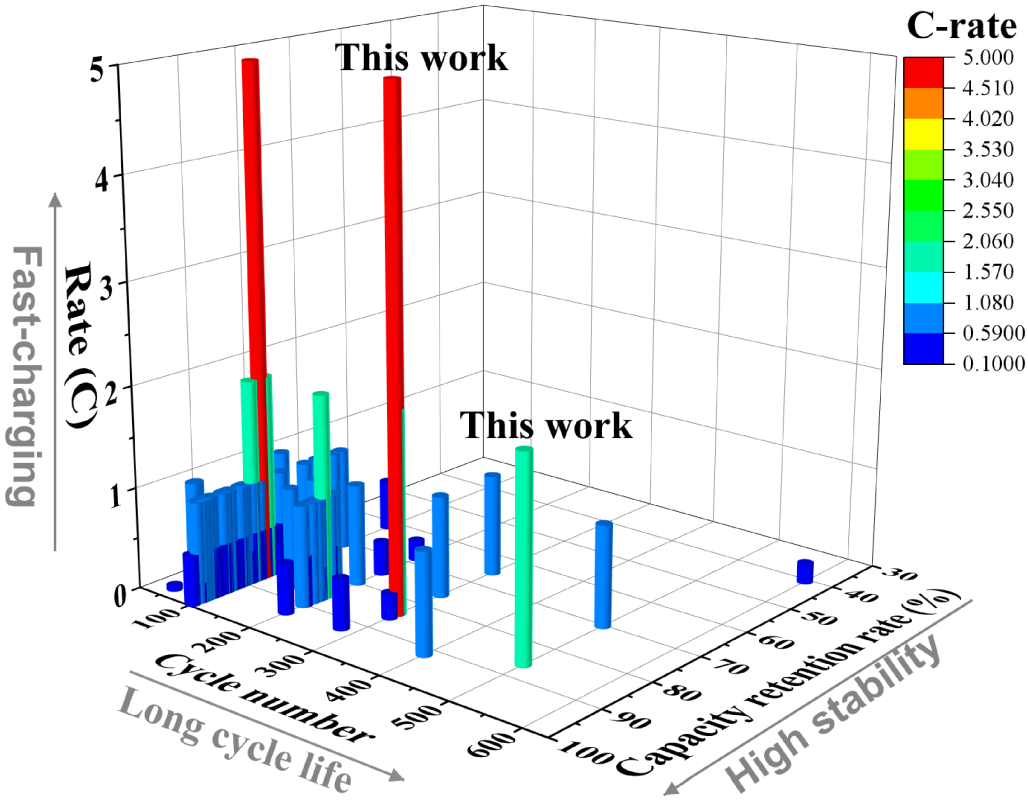

Supplementary Fig. 12 | Electrochemical performance comparison with reported polycrystalline ultrahigh-Ni (Ni > 90%) cathodes. The figure was plotted based on the data summarized from Supplementary Table 3, which includes > 100 papers published in the last 5 years (since 2018).

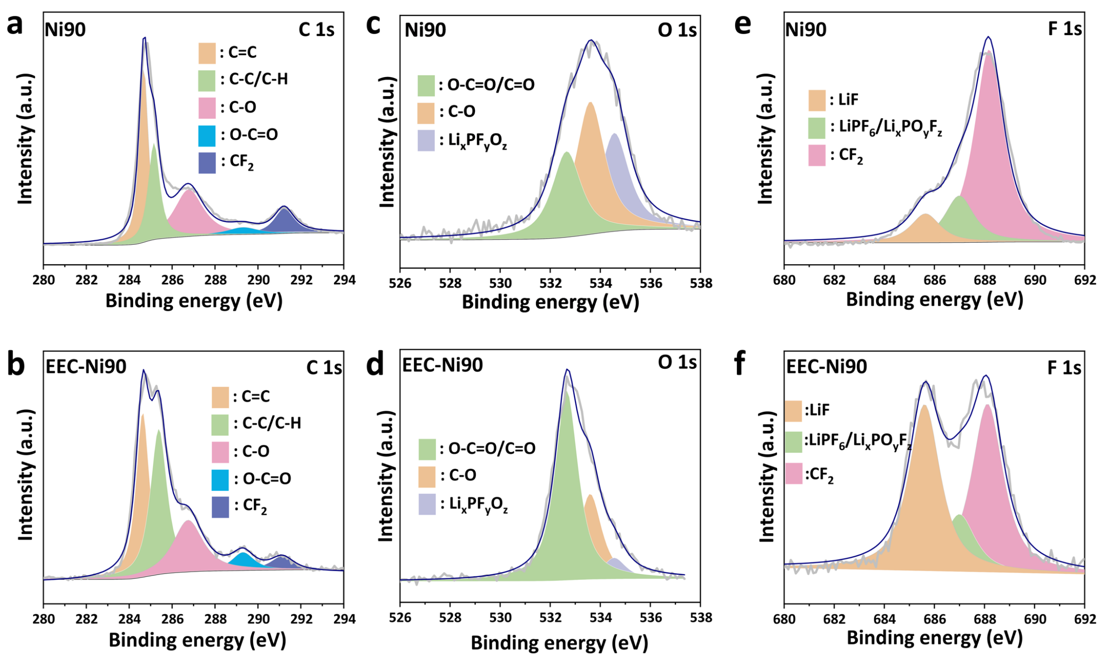

Supplementary Fig. 13 | X-ray photoelectron spectroscopy (XPS) characterization of Ni90 and EEC-Ni90 electrode after 30 cycles at 0.1C. XPS (a) C 1s, (c) O 1s and (e) F 1s spectra of cycled Ni90. XPS (b) C 1s, (d) O 1s and (f) F 1s spectra of cycled EEC-Ni90.

As shown in Supplementary Fig. S13a and S13b, the C 1s XPS spectra contains five peaks at 284.5, 285.3, 286.7, 289.3, and 291.1 eV. The peak located at 284.5 eV can be assigned to C=C bond that contributed from conductive carbon[1]. The peak located at 285.3 eV can be attributed to C-C/C-H species, including the contribution from polyvinylidene fluoride (PVDF) binder and decomposition product of ethylene carbonate (EC) during cycling[2,3]. The peak located at 286.7 eV can be assigned to C-O species from the EC polymerization[4]. The peak located at 289.3 eV can be assigned to O-C=O group associated to lithium carbonate/lithium alkyl carbonates, which is one important SEI/CEI component in carbonate-based electrolyte[3,5].

After cycling in GEN II electrolyte for 30 cycles, both Ni90 and EEC-Ni90 exhibited similar chemical compositions of the CEI layers. However, the CEI layer of EEC-Ni90 exhibited stronger C-C/C-H and O-C=O signals, suggesting the formation of more robust CEI layer on EEC-Ni90 compared to that of bare Ni90. More importantly, the XPS O 1s spectra (Supplementary Fig. S13c and S13d) also indicate that the EEC-Ni90 CEI layer exhibits stronger carbonate groups (O-C=O/C=O) signal than that of bare Ni90 without entropy-assisted coating layer, further confirming the formation of robust CEI layer on the surface of EEC-Ni90 cathode.

In addition, for the XPS F 1s spectra of cycled Ni90 and EEC-Ni90 (Supplementary

Fig. S13e and S13f), a much stronger LiF (685.5 eV)[6] signal was detected on the surface of EEC-Ni90 CEI layer, suggesting the entropy-assisted coating layer can induce the formation of F-rich CEI layer.

Therefore, based on the XPS characterization results of cycled Ni90 and EEC-Ni90 cathodes, it can be concluded that the entropy-assisted layer can induce the formation of robust CEI layer with higher content of O-C=O and LiF species compared to that of bare Ni90 cathode, which can thus effectively stabilize the interfacial properties of Ni-rich NCM cathode.

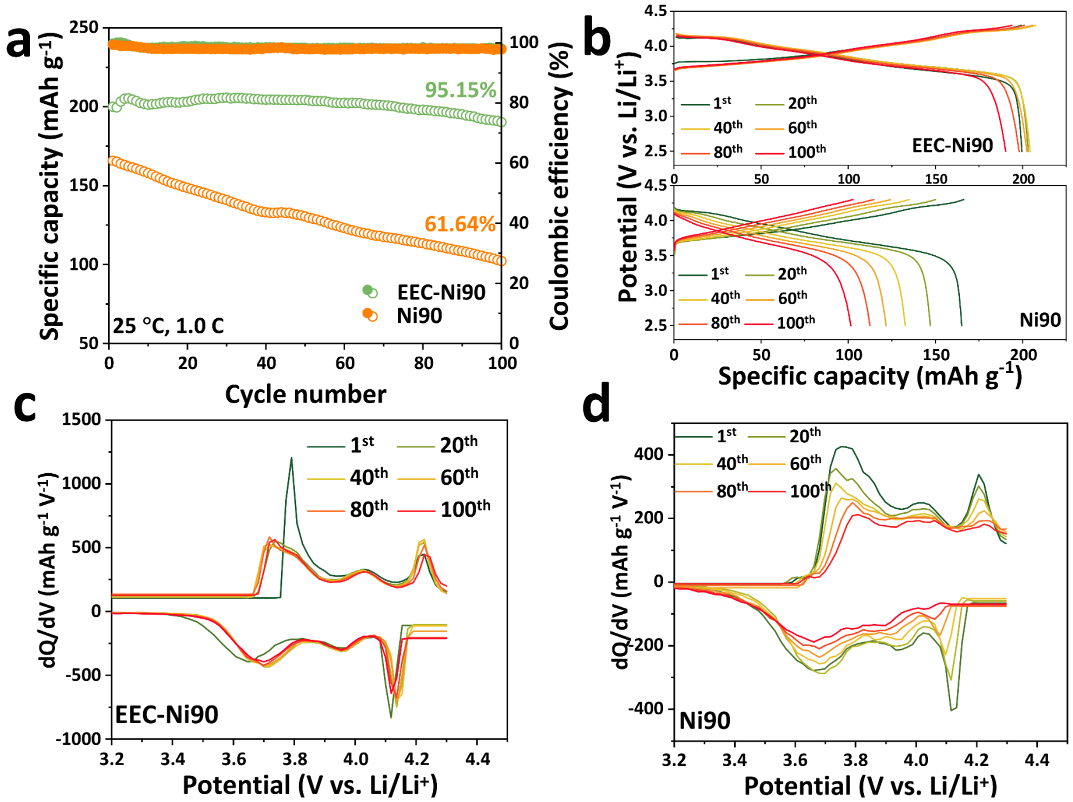

Supplementary Fig. 14 | The Electrochemical performance evaluation in Gen II electrolyte without VC additive. a-b, Cycling performance and voltage profiles of bare Ni90 and EEC-Ni90 cathode at 1.0C. The corresponding differential capacity (dQ/dV) curves of **c,** EEC-Ni90; and **d,** bare Ni90 cathode.

As illustrated in Supplementary Fig. 13a and 13b, even without VC additive, the EEC-Ni90 still demonstrated a significantly higher specific capacity (from 165.8 to 200.1 mAh g^{-1}) and capacity retention rate (from 61.64% to 95.15% for 100 cycles) than Ni90 during cycling at a charge/discharge rate of 1.0C. Moreover, the Ni90 suffered from obvious peak shifts and H2-H3 fading whereas EEC-Ni90 still exhibited a stable phase transition behavior during repeated charge/discharge (Supplementary Fig. 13c and 13d), confirming the effectiveness of the EEC layer in mitigating the surface-initiated structure degradation over cycling.

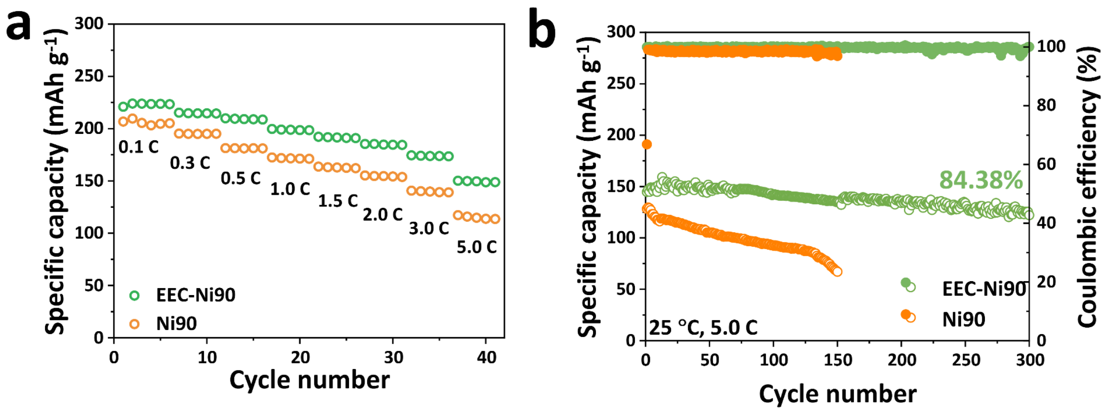

Supplementary Fig. 15 | a, Rate performance of bare Ni90 and EEC-Ni90 cathode in GEN II electrolyte. **b,** High-rate (5.0 C) cycling performance of bare Ni90 and EEC-Ni90 cathode in GEN II electrolyte.

The rate capability was evaluated under the rates ranging from 0.1C to 5.0C, which showed that the specific capacities of EEC-Ni90 at all C-rates were higher than those of Ni90 (Supplementary Fig. 14a). Additionally, EEC-Ni90 demonstrated better fast-charging stability with decent retention of 84.38% after 300 cycles at 5C (~ 12 minutes), whereas Ni90 showed rapid capacity fading within only 150 cycles (Supplementary Fig. 14b). The improved surface configurational entropy could possible narrow the interface band gap[7,8], enhancing the electron conductivity[9] to facilitate electron transportation under fast charging/discharging conditions.

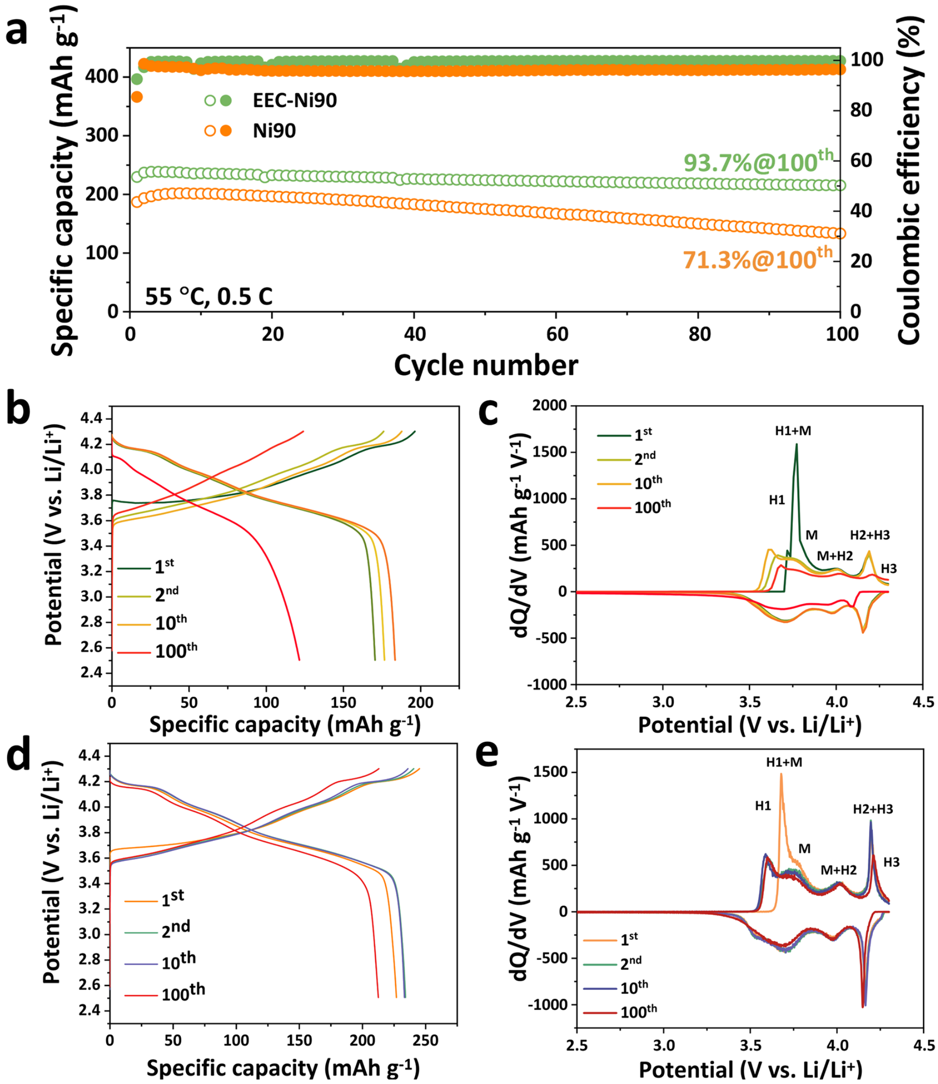

Supplementary Fig. 16 | High-temperature performance. a, Cycling performance of bare Ni90 and EEC-Ni90 cathdoe at 55 °C and 0.5C. **b-e,** The corresponding voltage profiles and differential capacity (dQ/dV) curves of bare Ni90 (b, c) and EEC-Ni90 cathode (d, e). The electrolyte is GENII without VC additive.

Wide temperature range performance of cathodes becomes critical due to increased battery usage under extreme conditions. However, elevated temperatures can induce more electrolyte/HF corrosion in cathode and hence faster degradation. As shown in Supplementary Fig. 15a, without the EEC layer, bare Ni90 could only deliver a 71.3% capacity retention rate after cycling at 55 °C for 100 cycles with rapid structural degradation (Supplementary Fig. 15b,c). By contrast, the capacity retention of EEC-Ni90 was dramatically improved to 93.7% after 100 cycles with better phase transition stability (Supplementary Fig. 15 d,e).

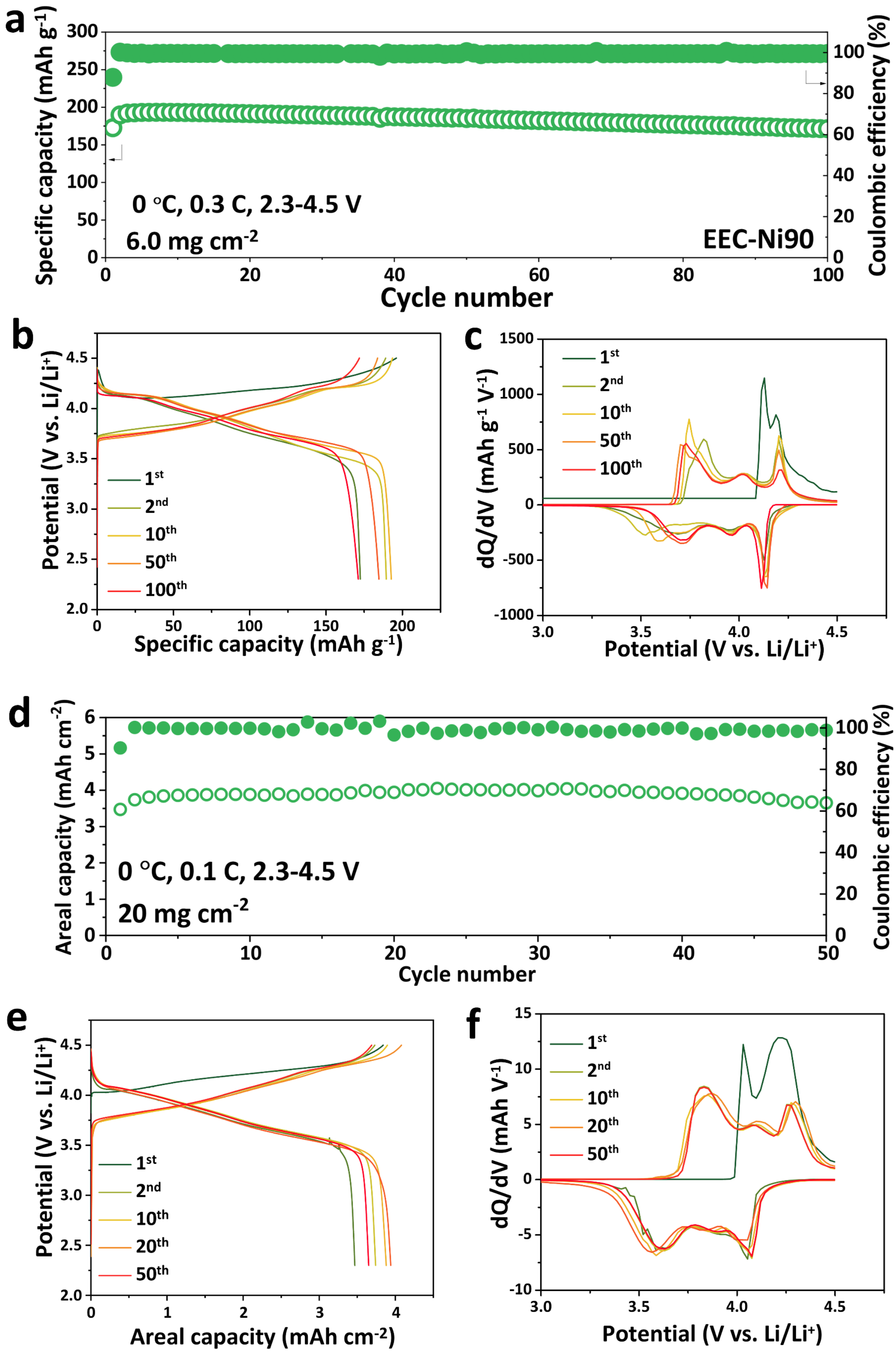

Supplementary Fig. 17 | Low-temperature performance. a, Cycling performance of EEC-Ni90 cathode at 0 °C and 0.3 C. **b-c,** The corresponding voltage profiles and differential capacity (dQ/dV) curves of EEC-Ni90 cathode in (a). **d,** Cycling performance of high areal loading (20 mg cm^{-2}) EEC-Ni90 cathode at 0 °C and 0.1 C. **e-f,** The corresponding voltage profiles and differential capacity (dQ/dV) curves in (d).

The electrolyte is GENII without VC additive.

The low temperature is often blamed for sluggish ionic transport in electrolytes and has been recently correlated with irreversible structural damage in cathode structures. When cycling at a lower temperature of 0 °C, EEC-Ni90 cathode could still deliver a reversible and stable capacity of > 170 mAh g^{-1} at 0.3C after 100 cycles (Supplementary Fig. 16 a-c). Moreover, even when tested under a high mass loading of 20 mg cm^{-2} and a higher charge cut-off voltage of 4.5 V, the cell could still deliver a high and reversible areal capacity of ~ 4.0 mAh cm^{-2} and stable cycle life at 0 °C (Supplementary Fig. 16 d-f).

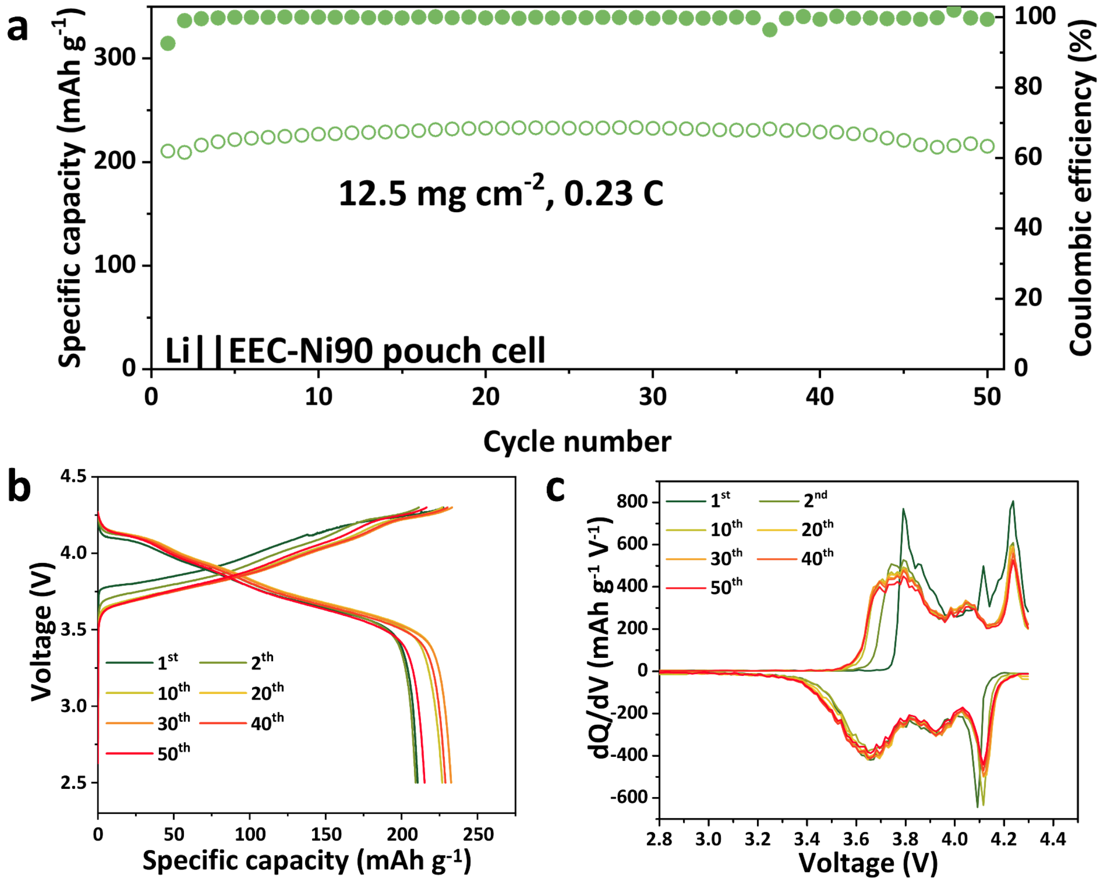

Supplementary Fig. 18 | a, Cycling performance of Li/EEC-Ni90 pouch cell at 0.23C. **b-c,** Voltage profiles and differential capacity (dQ/dV) curves of Li/EEC-Ni90 pouch cell at 0.23C. The electrolyte is GENII without VC additive.

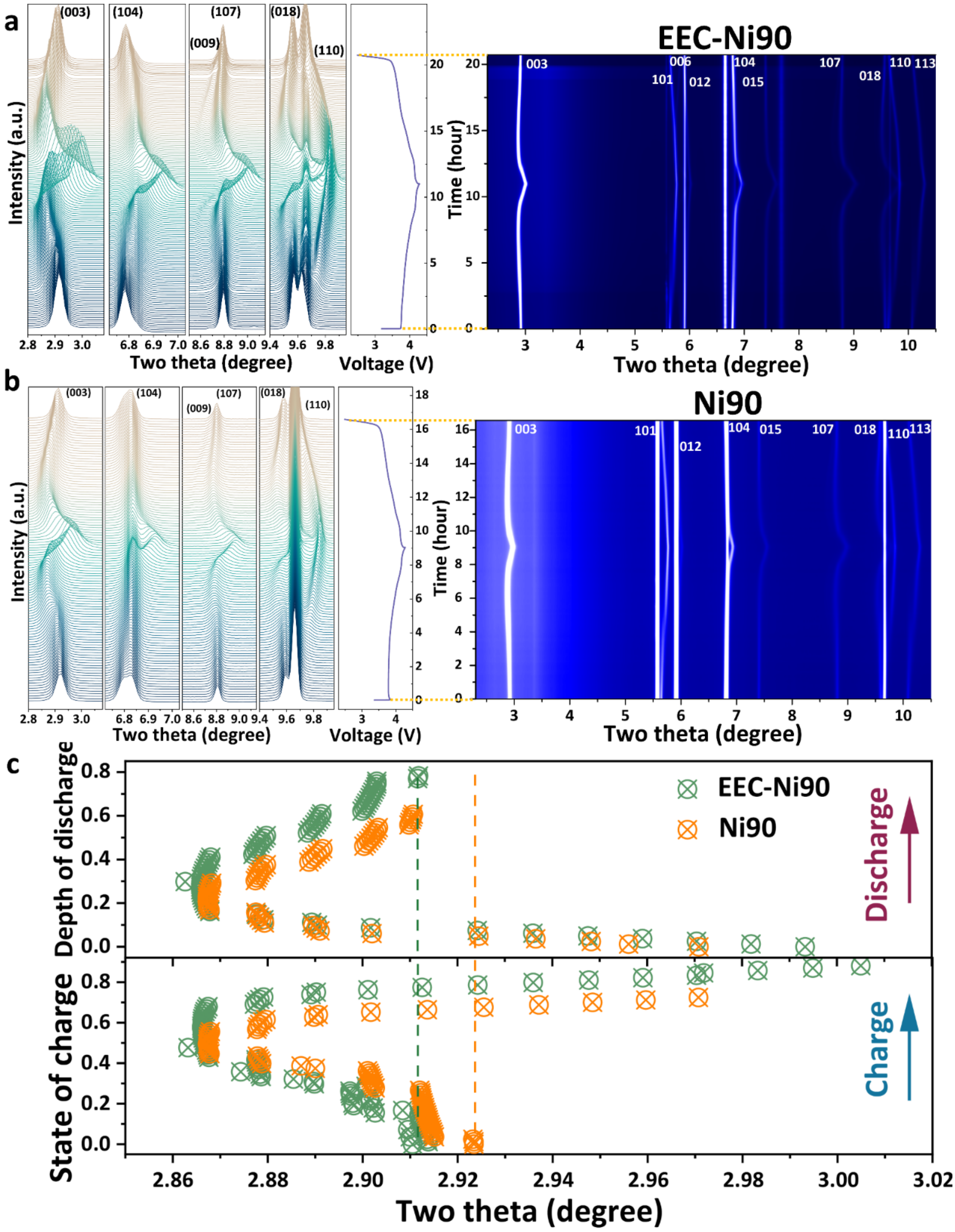

Supplementary Fig. 19 | Phase transition of EEC-Ni90 and Ni90 cathodes during the initial charge/discharge at 0.1C. a-b, Waterfall and 2D contour plot of in-situ HEXRD patterns at 0.1C. **c,** Two-theta evolution of (003) peaks for EEC-Ni90 and Ni90 cathodes during charge/discharge process.

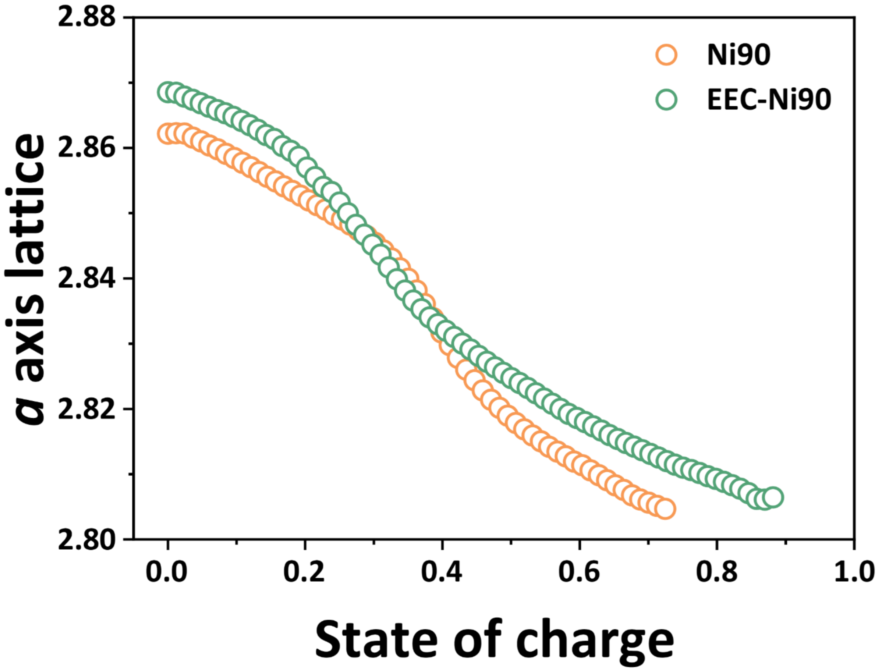

Supplementary Fig. 20 | Lattice parameter evolutions during the initial charge. Dynamic *a*-axis lattice parameters of Ni90 and EEC-Ni90 cathodes during the initial charge at 0.1C.

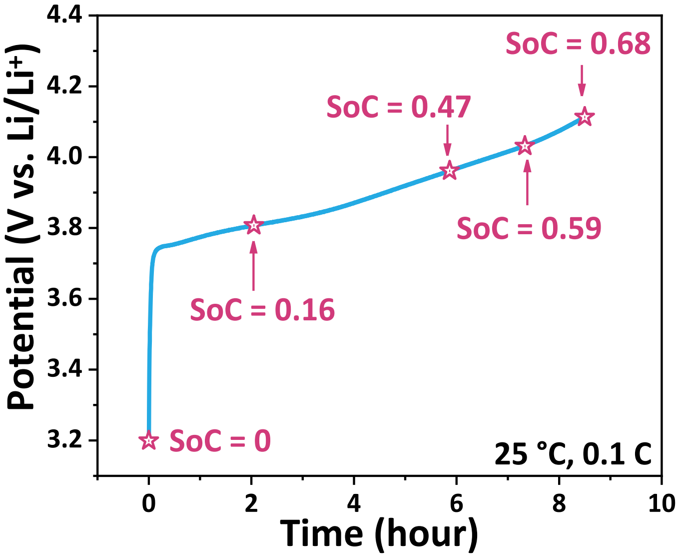

Supplementary Fig. 21 | The charge curve of EEC-90 cathode during in situ BCDI measurement.

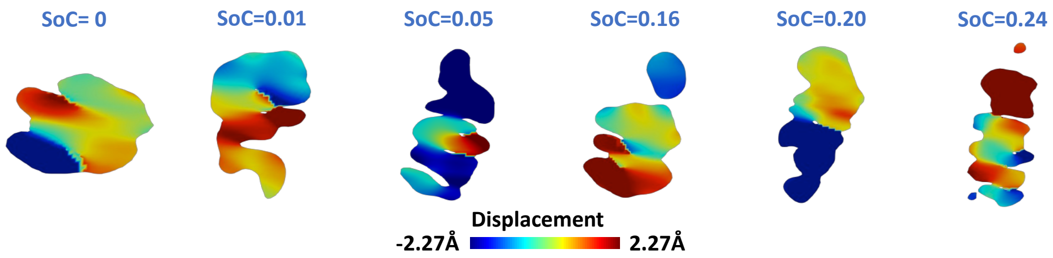

Supplementary Fig. 22 | In situ BCDI images of Ni90 cathode in the atomic displacement field at different SoC.

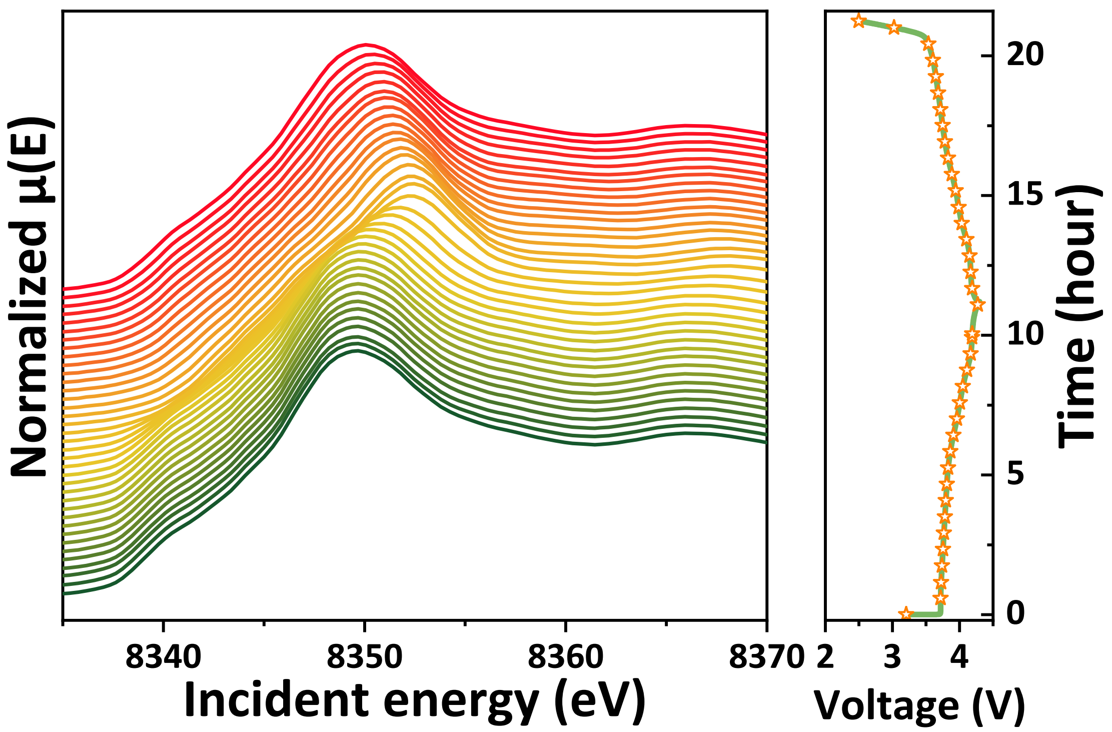

Supplementary Fig. 23| In-situ Ni K-edge XANES results of EEC-Ni90 cathode during the initial cycle combined with the corresponding charge/discharge voltage profiles. The star marks in the voltage profiles corresponding to the XAS data collection points.

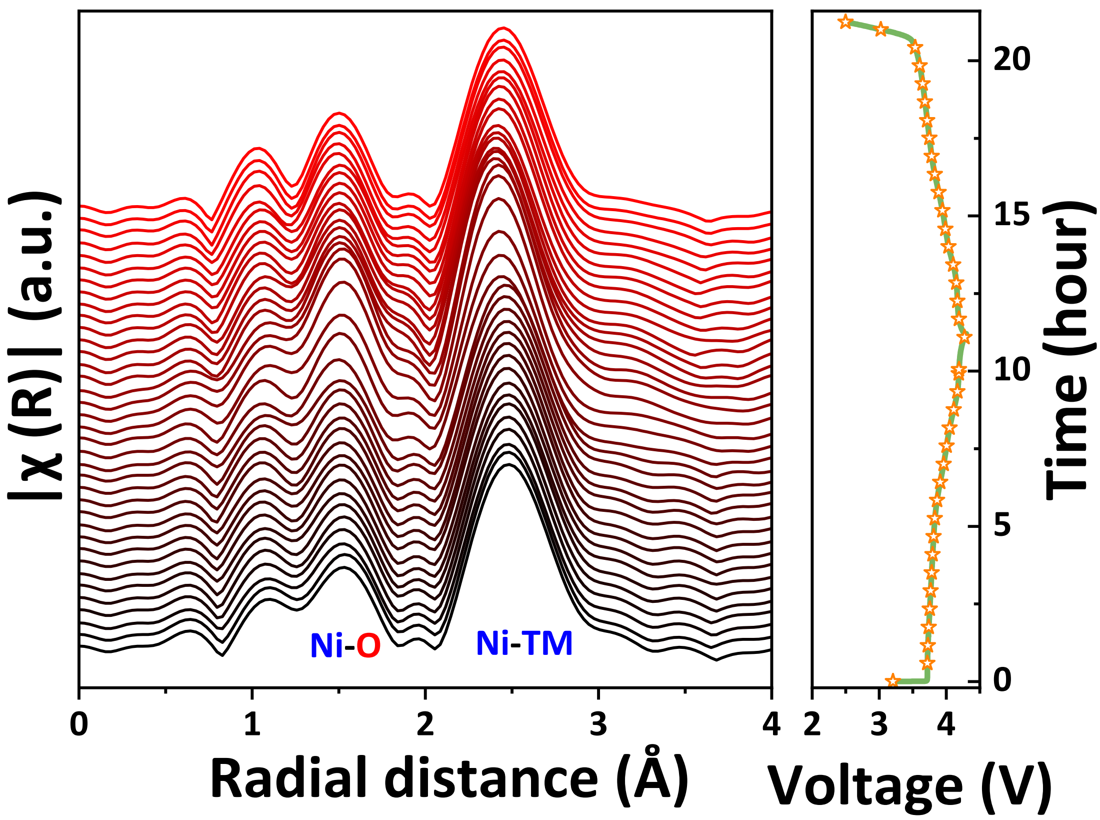

Supplementary Fig. 24 | In-situ Ni K-edge EXAFS spectra of EEC-Ni90 cathode during initial cycle combined with corresponding charge/discharge voltage profiles. The star marks in the voltage profiles corresponding to the XAS data collection points.

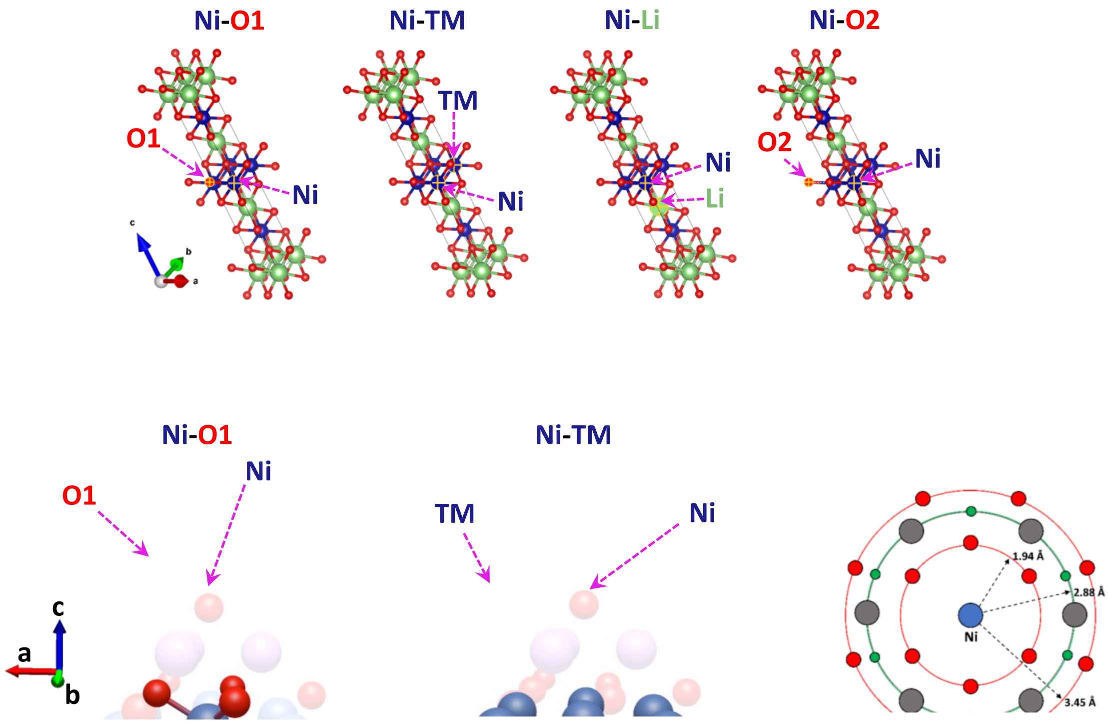

Supplementary Fig. 25 | EXAFS fitting model. a, Schematic illustration of the crystal structure model used for the in-situ EXAFS fitting. **b,** Schematic illustration of the X-ray scattering paths used for in-situ EXAFS fitting.

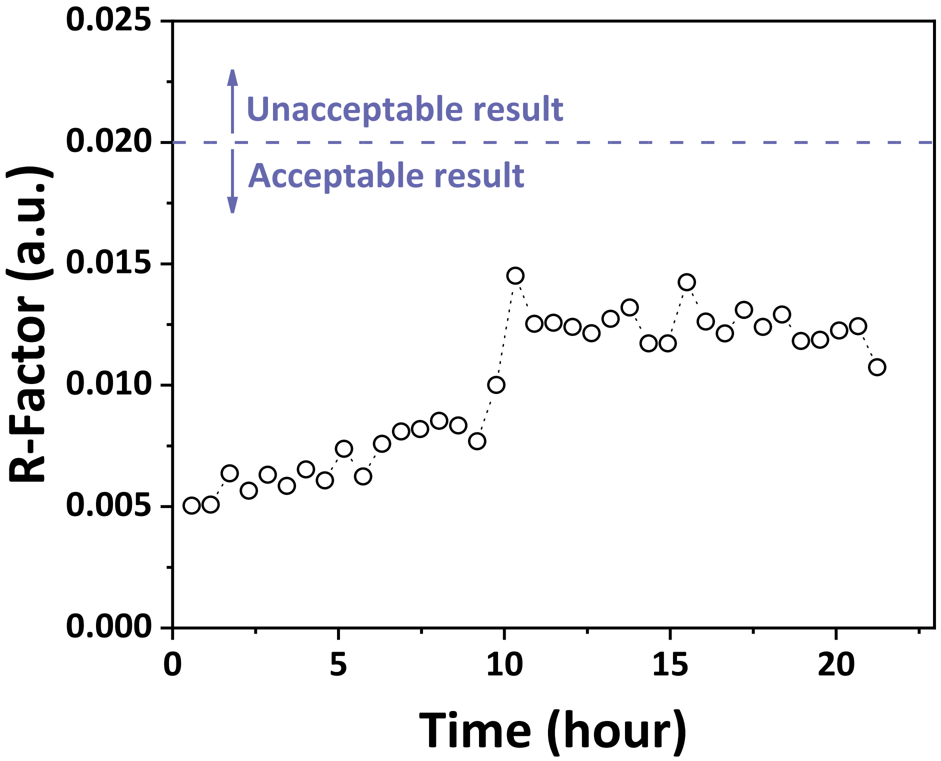

Supplementary Fig. 26 | Corresponding R-factor of the in-situ EXAFS fitting results.

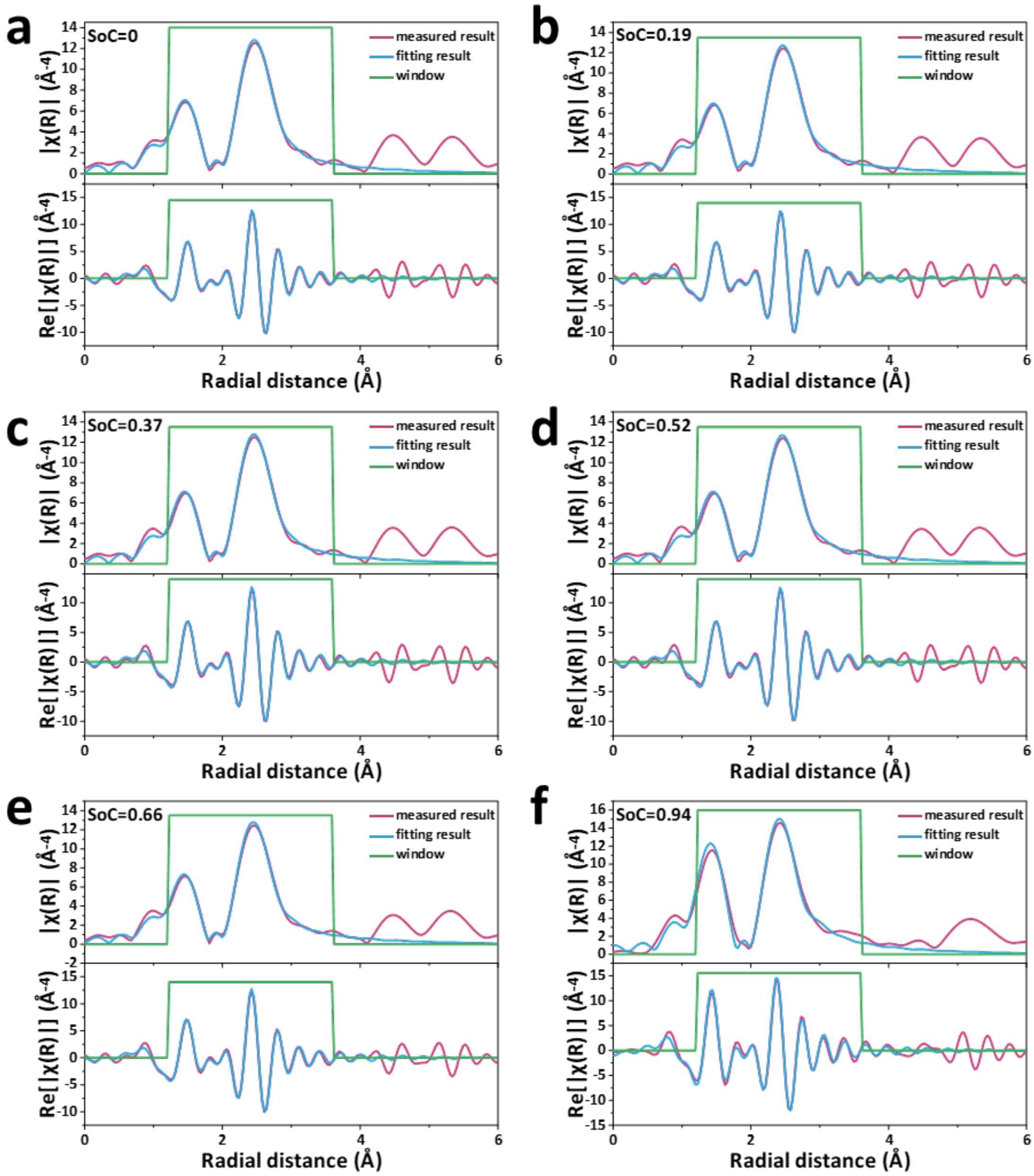

Supplementary Fig. 27 | EXAFS fitting results at different SoC. Selected in-situ EXAFS fitting details for EEC-Ni90 cathode during initial charging process at various SoC: **a,** SoC = 0; **b,** SoC = 0.19; **c,** SoC = 0.37; **d,** SoC = 0.52; **e,** SoC = 0.63; **f,** SoC = 0.94.

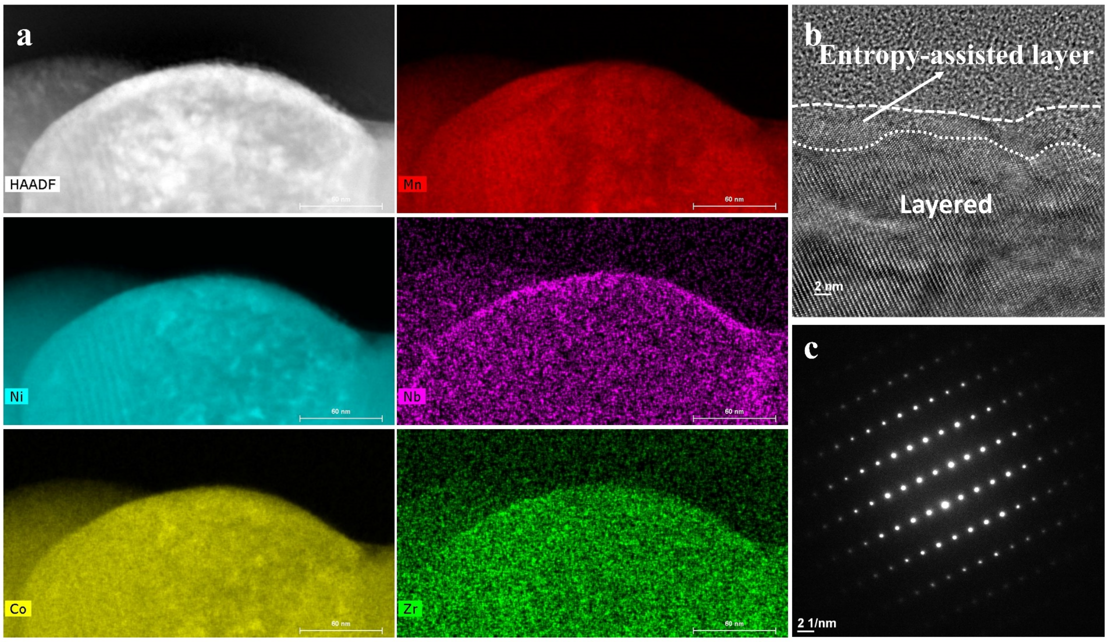

Supplementary Fig. 28 | TEM characterization of EEC-Ni90 cathode after cycling at 1.0C for 100 cycles. a, HAADF-STEM elemental mapping. **b,** HRTEM image. **c,** SAED pattern. The corresponding electrochemical cycling performance combined with the voltage profiles at different cycles are shown in Supplementary Fig. 28. The electrolyte is GENII without VC additive.

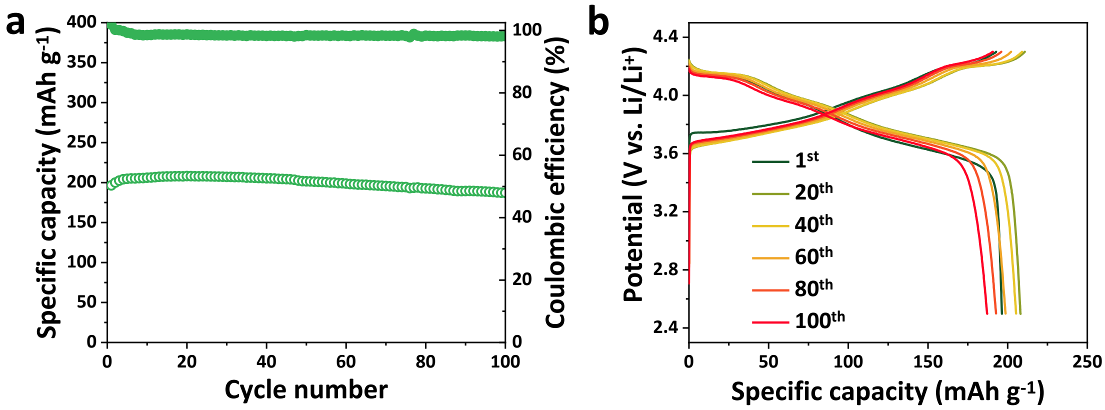

Supplementary Fig. 29 | a, Cycling performance and **b,** Voltage profiles of EEC-Ni90 cathode at 1C for the TEM test as shown in Supplementary Fig. 27. The electrolyte is GENII without VC additive.

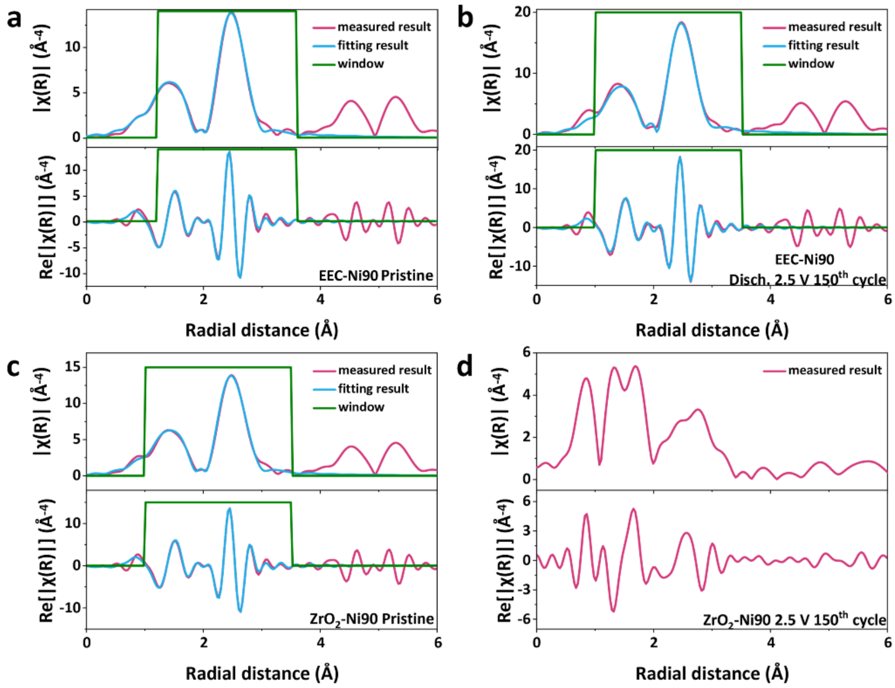

Supplementary Fig. 30 | Ex-situ EXAFS fitting details. EXAFS fitting details of **a,** pristine EEC-Ni90 cathode; **b,** cycled EEC-Ni90 cathode (150 cycles at 0.5C and 55 °C) at discharged state (2.5 V); **c,** EXAFS fitting of pristine ZrO_2-Ni90 cathode. **d,** EXAFS spectra of cycled ZrO_2-Ni90 cathode (150 cycles at 0.5C and 55 °C) at discharged state (2.5 V). Because of the severe phase transformation, the EXAFS fitting cannot be conducted for cycled ZrO_2-Ni90 cathode.

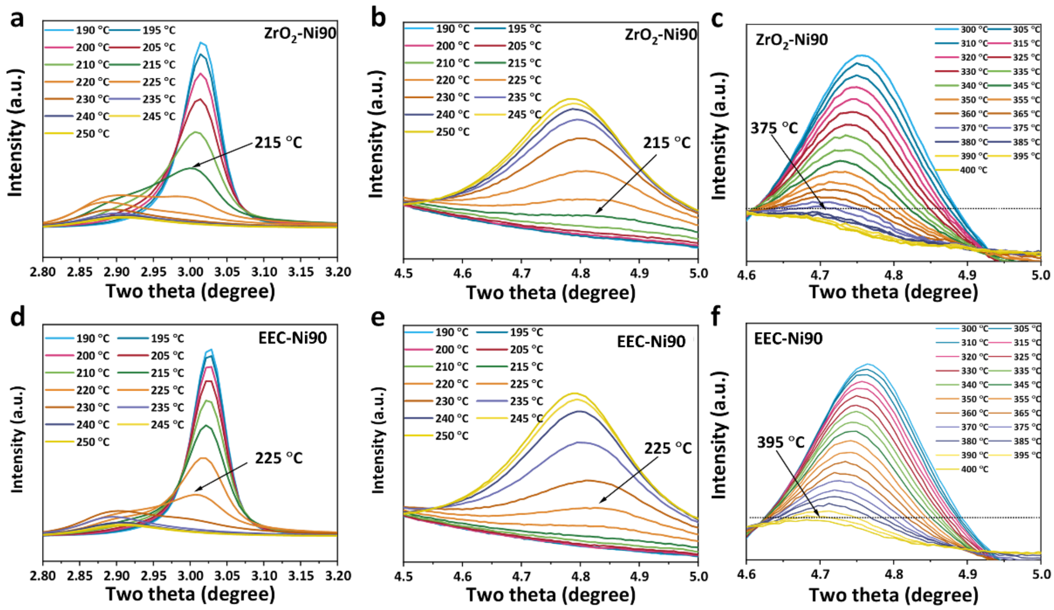

Supplementary Fig. 31 | Detailed in-situ HEXRD patterns during heating. (a-c) 4.3V-charged ZrO_2-Ni90 cathode; (**d-f)** 4.3V-charged EEC-Ni90 cathode.

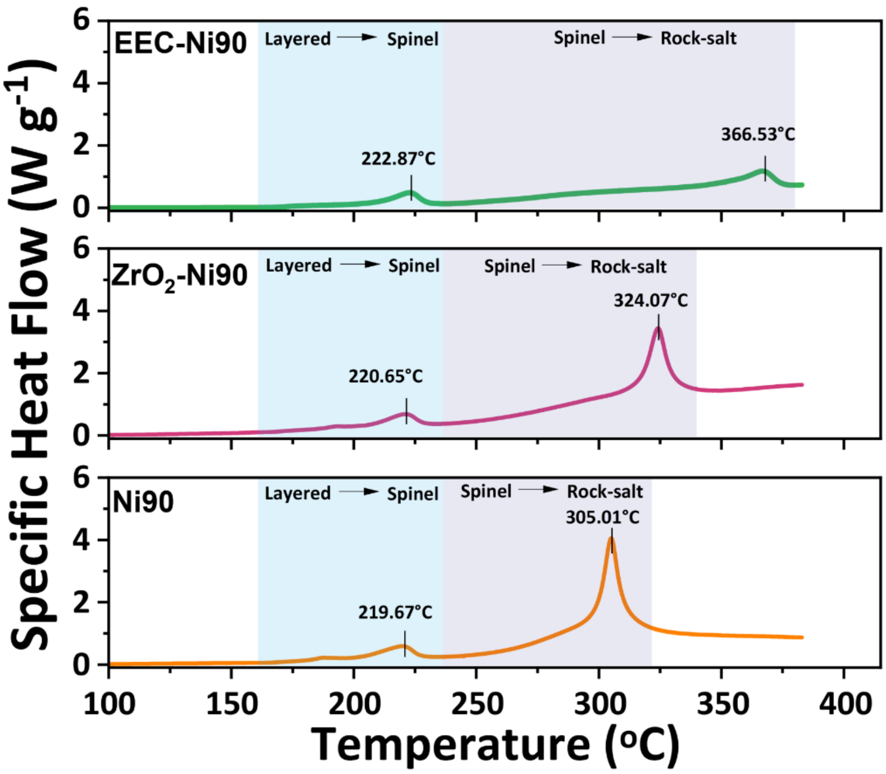

Supplementary Fig. 32 | DSC profiles of electrochemically delithiated Ni90, ZrO_2-Ni90, and EEC-Ni90 cathodes. The delithiation capacities for all samples were controlled to be 220 mAh g^{-1}.

Supplementary Table 1. Lattice parameters of bare Ni90 obtained from HEXRD Rietveld refinement

Sample		**Ni90**			
Crystal system		**Rhombohedral**			
Space group		**R – 3m**			
Atom	**Mult**	**x**	**Y**	**z**	**Site fraction**
Li1	3	0	0	0	0.9435
Ni2	3	0	0	0	0.0565
Li2	3	0	0	0.5	0.0565
Ni1	3	0	0	0.5	0.8435
Co1	3	0	0	0.5	0.05
Mn1	3	0	0	0.5	0.05
O1	6	0	0	0.2417	1
$a = b$		2.87224 Å			
c		14.1804 Å			
Li/Ni disorder		5.65%			
R_{wp}		8.051%			

Supplementary Table 2. Lattice parameters of EEC-Ni90 obtained from HEXRD Rietveld refinement

Sample		**EEC-Ni90**			
Crystal system		**Rhombohedral**			
Space group		**R – 3m**			
Atom	**Mult**	**x**	**Y**	**z**	**Site fraction**
Li1	3	0	0	0	0.9899
Ni2	3	0	0	0	0.0101
Li2	3	0	0	0.5	0.0101
Ni1	3	0	0	0.5	0.8899
Co1	3	0	0	0.5	0.05
Mn1	3	0	0	0.5	0.05
O1	6	0	0	0.2417	1
$a = b$		2.87455 Å			
c		14.19792 Å			
Li/Ni disorder		1.01%			
R_{wp}		7.537%			

Supplementary Table 3. Summary of recently reported ultrahigh-Ni (Ni content > 0.9) polycrystalline cathodes using Li metal anode

Composition	Electrolyte	Voltage range	Rate	Areal loading	Retention rate @ cycle number	Ref
$LiNi_{0.90}Co_{0.05}Mn_{0.05}O_2$	**1.2 M $LiPF_6$ in EC/EMC (3/7)**	**2.5 – 4.3 V**	**1.0 C**	**6.0 mg cm^{-2}**	**95.1% @100**	**This work**
$LiNi_{0.90}Co_{0.05}Mn_{0.05}O_2$	**1.2 M $LiPF_6$ in EC/EMC (3/7)**	**2.5 – 4.3 V**	**5.0 C**	**4.0 mg cm^{-2}**	**84.3% @300**	**This work**
$LiNi_{0.90}Co_{0.05}Mn_{0.05}O_2$	**1.2 M $LiPF_6$ in EC/EMC (3/7) with 2 wt.% VC additive**	**2.0 – 4.3 V**	**1.0 C**	**4.0 mg cm^{-2}**	**96.0% @200**	**This work**
$LiNi_{0.90}Co_{0.05}Mn_{0.05}O_2$	**1.2 M $LiPF_6$ in EC/EMC (3/7) with 2 wt.% VC additive**	**2.0 – 4.4 V**	**2.0 C**	**4.0 mg cm^{-2}**	**86.2% @500**	**This work**
$LiNi_{0.90}Co_{0.09}Ta_{0.01}O_2$	1.2 M $LiPF_6$ in EC/EMC (3/7) with 2 wt.% VC additive	2.7 – 4.3 V	0.5 C	4 – 5 mg cm^{-2}	95% @ 100	*Nat. Energy* **2020**[10]
$LiNi_{0.89}Mn_{0.1}Mo_{0.01}O_2$	1.2 M $LiPF_6$ in EC/EMC (3/7) with 2 wt.% VC additive	2.7 – 4.4 V	0.5 C	4 – 5 mg cm^{-2}	92.8% @100	*Nat. Energy* **2022**[11]
$LiNi_{0.90}Co_{0.05}Mn_{0.05}O_2$	1.2 M $LiPF_6$ in EC/EMC (3/7) with 2 wt.% VC additive	2.7 – 4.4 V	0.5 C	4 – 5 mg cm^{-2}	83.9% @100	*Nat. Energy* **2022**[11]
$LiNi_{0.90}Mn_{0.1}O_2$	1.2 M $LiPF_6$ in EC/EMC (3/7) with 2 wt.% VC additive	2.7 – 4.4 V	0.5 C	4 – 5 mg cm^{-2}	87.7% @100	*Nat. Energy* **2022**[11]
$LiNi_{0.91}Co_{0.09}O_2$	1.2 M $LiPF_6$ in EC/EMC (3/7) with 2 wt.% VC additive	3.0 – 4.2 V	1.0 C	4 – 5 mg cm^{-2}	97% @100	*Nat. Common.* **2021**[12]
$LiNi_{0.9}Co_{0.1}O_2$	1.2 M $LiPF_6$ in EC/EMC (3/7) with 2 wt.% VC additive	2.7 – 4.3 V	1.0 C	N/A	97.4% @100	*Nat. Common.* **2021**[13]
$LiNi_{0.90}Co_{0.06}Mn_{0.04}O_2$	1.0 M $LiPF_6$ in EC/DMC/DEC (1/1/1)	3.0 – 4.3 V	1.0 C	N/A	~ 87% @ 100	*Adv. Mater.* **2022**[14]
$LiNi_{0.94}Co_{0.04}Mn_{0.02}O_2$	1.2 M $LiPF_6$ in EC/EMC (3/7) with 2 wt.% VC additive	2.7 – 4.2 V	0.5 C	4 – 5 mg cm^{-2}	94.8% @ 100	*Adv. Energy Mater.* **2023**[15]
$LiNi_{0.92}Co_{0.04}Mn_{0.04}O_2$	1.0 M $LiPF_6$ in EC/DMC/DEC (1/1/1)	2.7 – 4.3 V	0.2 C	3.5 mg cm^{-2}	40.74% @ 600	*Adv. Energy Mater.* **2022**[16]
$LiNi_{0.90}Mn_{0.05}Co_{0.05}O_2$	1.2 M $LiPF_6$ in EC/EMC (3/7) with 2 wt.% VC additive	3.0 – 4.2 V	0.5 C	4 – 5 mg cm^{-2}	93.4% @ 100	*Adv. Energy Mater.* **2021**[17]
$LiNi_{0.9}Co_{0.1}O_2$	1.2 M $LiPF_6$ in EC/EMC (3/7) with 2 wt.% VC additive	2.7 – 4.3 V	0.5 C	4 – 5 mg cm^{-2}	78.8% @ 100	*Adv. Energy Mater.* **2020**[18]
$LiNi_{0.90}Co_{0.09}W_{0.01}o_2$	1.2 M $LiPF_6$ in EC/EMC (3/7) with 2 wt.% VC additive	2.7 – 4.3 V	1.0 C	4 – 5 mg cm^{-2}	96% @100	*Adv. Energy Mater.* **2019**[19]
$LiNi_{0.90}Mn_{0.05}Co_{0.05}O_2$	1.2 M $LiPF_6$ in EC/EMC (3/7) with 2 wt.% VC additive	2.7 – 4.3 V	0.5 C	4 mg cm^{-2}	91% @ 100	*Adv. Energy Mater.* **2018**[20]
$LiNi_{0.9}Mn_{0.1}O_2$	1.2 M $LiPF_6$ in EC/EMC (3/7) with 2 wt.% VC additive	2.7 – 4.3 V	0.5 C	4 mg cm^{-2}	93% @ 100	*Adv. Energy Mater.* **2020**[21]
$LiNi_{0.90}Mn_{0.05}Co_{0.05}O_2$	1.2 M $LiPF_6$ in EC/EMC (3/7) with 2 wt.% VC additive	2.7 – 4.3 V	0.5 C	4 – 5 mg cm^{-2}	92.2% @100	*Adv. Energy Mater.* **2019**[22]

$LiNi_{0.92}Co_{0.04}Mn_{0.04}O_2$	1.2 M $LiPF_6$ in EC/EMC (3/7)	2.5 – 4.5 V	0.3 C	8.0 mg cm^{-2}	78% @100	*Adv. Funct. Mater.* **2021**[23]
$LiNi_{0.9}Co_{0.0.9}Mo_{0.01}O_2$	1.2 M $LiPF_6$ in EC/EMC (3/7)	2.7 – 4.3 V	1.0 C	5 mg cm^{-2}	92.3% @100	*Angew. Chem.* **2023**[24]
$LiNi_{0.90}Co_{0.05}Mn_{0.05}O_2$	1.0 M $LiPF_6$ in EC/DMC (1/1)	2.8 – 4.4 V	0.33 C	13.1 mg cm^{-2}	75.3% @200	*Chem. Mater.* **2022**[25]
$LiNi_{0.90}Co_{0.05}Mn_{0.05}O_2$	1.2 M $LiPF_6$ in EC/EMC (3/7) with 1 wt.% VC additive	2.7 – 4.3 V	0.5 C	N/A	87% @100	*Chem. Mater.* **2017**[26]
$LiNi_{0.95}Co_{0.025}Mn_{0.025}O_2$	1.2 M $LiPF_6$ in EC/EMC (3/7) with 2 wt.% VC additive	2.7 – 4.3 V	0.5 C	N/A	~ 82% @100	*Chem. Mater.* **2018**[27]
$LiNi_{0.90}Co_{0.05}Mn_{0.05}O_2$	1.2 M $LiPF_6$ in EC/EMC (3/7) with 2 wt.% VC additive	2.7 – 4.3 V	0.5 C	N/A	~ 84% @100	*Chem. Mater.* **2018**[27]
$LiNi_{0.95}Mg_{0.05}O_2$	1.0 M $LiPF_6$ in EC/DEC (1/2) with 1 wt.% DTD additive	3.0 – 4.3 V	0.05 C	10 – 12 mg cm^{-2}	97.33% @50	*Chem. Mater*. **2019**[28]
$LiNi_{0.9}Co_{0.05}Mn_{0.05}O_2$	1.0 M $LiPF_6$ in EC/DEC (1/1)	2.7 – 4.3 V	1.0 C	6 mg cm^{-2}	88.56% @200	*ACS Appl. Energy Mater.* **2021**[29]
$LiNi_{0.9}Co_{0.1}O_2$	1.0 M $LiPF_6$ in EC/EMC/DMC (1/1/1)	2.75 – 4.3 V	0.2 C	N/A	84.41% @100	*ACS Appl. Mater. Interfaces* **2020**[30]
$LiNi_{0.9}Co_{0.05}Mn_{0.05}O_2$	1.0 M $LiPF_6$ in EC/DEC (3/7) with 0.3 wt.% HTZ additive	3.0 – 4.3 V	1.0 C	3 – 4 mg cm^{-2}	86.6% @150	*ACS Appl. Mater. Interfaces* **2021**[31]
$LiNi_{0.92}Co_{0.08}O_2$	1.0 M $LiPF_6$ in EC/EMC/DMC (1/1/1)	2.75 – 4.3 V	0.2 C	N/A	93.8% @100	*ACS Appl. Mater. Interfaces* **2021**[32]
$LiNi_{0.92}Co_{0.05}Mn_{0.03}O_2$	1.0 M $LiPF_6$ in EC/DMC (1/1)	2.7 – 4.3 V	1.0 C	5.0 mg cm^{-2}	78.3% @100	*ACS Appl. Mater. Interfaces* **2021**[33]
$LiNi_{0.9}Co_{0.07}Mn_{0.01}Al_{0.02}O_2$	1.0 M $LiPF_6$ in EC/EMC/DMC (1/1/1)	2.7 – 4.3 V	1.0 C	2.6 mg cm^{-2}	88.3% @100	*ACS Appl. Mater. Interfaces* **2021**[34]
$LiNi_{0.91}Co_{0.06}Mn_{0.03}O_2$	1.0 M $LiPF_6$ in FEC/DMC	3.0 – 4.3 V	1.0 C	10 mg cm^{-2}	93.44% @50	*ACS Appl. Mater. Interfaces* **2018**[35]
$LiNi_{0.9}Co_{0.05}Mn_{0.05}O_2$	1.2 M $LiPF_6$ in EC/EMC (3/7) with 2 wt.% VC additive	2.7 – 4.3 V	0.5 C	4 – 5 mg cm^{-2}	88.4% @100	*ACS Appl. Mater. Interfaces* **2019**[36]
$LiNi_{0.9}Co_{0.045}Mn_{0.045}Al_{0.01}O_2$	1.2 M $LiPF_6$ in EC/EMC (3/7) with 2 wt.% VC additive	2.7 – 4.3 V	0.5 C	4 mg cm^{-2}	95% @100	*ACS Energy Lett.* **2021**[37]
$LiNi_{0.9}Co_{0.05}Mn_{0.05}O_2$	1.0 M $LiPF_6$ in EC/DMC (1/1)	2.7 – 4.3 V	2.0 C	2 – 5 mg cm^{-2}	88.2% @100	*ACS Appl. Mater. Interfaces* **2020**[38]
$LiNi_{0.9}Co_{0.05}Mn_{0.05}O_2$	1.2 M $LiPF_6$ in EC/EMC (3/7) with 2 wt.% VC additive	2.7 – 4.3 V	0.5 C	4 – 5 mg cm^{-2}	90% @100	*ACS Energy Lett.* **2021**[39]
$LiNi_{0.9}Co_{0.05}Mn_{0.05}O_2$	1.2 M $LiPF_6$ in EC/EMC (3/7) with 2 wt.% VC additive	2.7 – 4.3 V	0.5 C	4 – 5 mg cm^{-2}	87% @100	*ACS Energy Lett.* **2022**[40]

$LiNi_{0.9}Co_{0.05}Mn_{0.05}O_2$	1.2 M $LiPF_6$ in EC/EMC (3/7) with 2 wt.% VC additive	2.7 – 4.3 V	0.5/1.0 C Ch./Disch.	9.5 – 10 mg cm^{-2}	92.5% @280	*ACS Energy Lett.* **2022**[41]
$LiNi_{0.9}Co_{0.05}Mn_{0.05}O_2$	1.2 M $LiPF_6$ in EC/EMC (3/7) with 2 wt.% VC additive	2.7 – 4.3 V	0.5 C	5.0 mg cm^{-2}	80.7% @50	*ACS Nano* **2020**[42]
$LiNi_{0.9}Mn_{0.1}O_2$	1.0 M $LiPF_6$ in EC/DMC (1/1)	3.0 – 4.3 V	1.0 C	3.0 mg cm^{-2}	65.53% @300	*ACS Sustain. Chem. Eng.* **2022**[43]
$LiNi_{0.9}Co_{0.05}Mn_{0.05}O_2$	N/A	2.8 – 4.3 V	1.0 C	N/A	92.3% @100	*ACS Sustain. Chem. Eng.* **2022**[44]
$LiNi_{0.93}Co_{0.03}Mn_{0.03}Al_{0.01}O_2$	1.2 M $LiPF_6$ in EC/EMC (3/7) with 2 wt.% VC additive	2.7 – 4.3 V	0.5 C	4 – 5 mg cm^{-2}	86.9% @100	*ACS Energy Lett.* **2023**[45]
F-Sb-$LiNi_{0.93}Co_{0.03}Mn_{0.03}Al_{0.01}O_2$	1.2 M $LiPF_6$ in EC/EMC (3/7) with 2 wt.% VC additive	2.7 – 4.3 V	0.5 C	4 – 5 mg cm^{-2}	99.3% @100	*ACS Energy Lett.* **2023**[45]
$LiNi_{0.9}Co_{0.07}Al_{0.03}O_2$	1.15 M $LiPF_6$ in EC/DMC/EMC (1/2/2)	2.8 – 4.3 V	2.0 C	5 mg cm^{-2}	86.3% @200	*J. Mater. Chem. A* **2017**[46]
$LiNi_{0.9}Co_{0.05}Mn_{0.05}O_2$	1.2 M $LiPF_6$ in EC/EMC (3/7) with 2 wt.% VC additive	2.7 – 4.3 V	0.5 C	4 mg cm^{-2}	93% @100	*J. Mater. Chem. A* **2019**[47]
$LiNi_{0.9}Co_{0.06}Mn_{0.04}O_2$	1.0 M $LiPF_6$ in EC/EMC/DMC (1/1/1)	2.75 – 4.3 V	1.0 C	N/A	~76% @100	*ChemSusChem* **2021**[48]
$LiNi_{0.92}Co_{0.03}Mn_{0.03}Al_{0.02}O_2$	1.0 M $LiPF_6$ in EC/EMC (3/7) with 2 wt.% VC additive	2.7 – 4.3 V	0.5 C	N/A	92% @100	*J. Mater. Chem. A* **2020**[49]
$LiNi_{0.95}Co_{0.04}Mn_{0.01}O_2$	1.2 M $LiPF_6$ in EC/EMC (3/7) with 2 wt.% VC additive	2.7 – 4.3 V	0.5 C	4 – 5 mg cm^{-2}	91% @100	*Energy Environ. Sci.* **2021**[50]
$LiNi_{0.9}Co_{0.1}O_2$	1.0 M $LiPF_6$ in EC/EMC (3/7) with 2 wt.% VC additive	3.0 – 4.3 V	0.33 C	5 mg cm^{-2}	95% @100	*J. Mater. Chem. A* **2023**[51]
$Li_{0.994}Mg_{0.006}(Ni_{0.925}Co_{0.03}Mn_{0.045})_{0.996}Zr_{0.004}O_2$	1.0 M $LiPF_6$ in EC/EMC/EMC (1/1/1)	2.8 – 4.3 V	1.0 C	N/A	82.03% @150	*J. Energy Storage* **2023**[52]
$LiNi_{0.9}Co_{0.1}O_2$	1.0 M $LiPF_6$ in EC/EMC (3/7)	2.75 – 4.3 V	1.0 C	N/A	93% @100	*Chem. Phys. Lett.* **2019**[53]
$LiNi_{0.9}Co_{0.1}O_2$	1.0 M $LiPF_6$ in EC/EMC/DMC (1/1/1)	2.8 – 4.3 V	0.5 C	5 mg cm^{-2}	85.7% @100	*Electrochem. Acta* **2022**[54]
$LiNi_{0.91}Co_{0.06}Mn_{0.03}O_2$	1.0 M $LiPF_6$ in EC/EMC/DMC (1/1/1)	3.0 – 4.3 V	0.5 C	N/A	83.9% @80	*Electrochem. Acta* **2021**[55]
$LiNi_{0.9}Co_{0.05}Mn_{0.04}Al_{0.01}O_2$	1.0 M $LiPF_6$ in EC/EMC/DMC (1/1/1)	2.8 – 4.3 V	0.2 C	7 mg cm^{-2}	95.1% @100	*Electrochem. Acta* **2023**[56]
$LiNi_{0.9}Co_{0.04}Mn_{0.03}Al_{0.03}O_2$	1.0 M $LiPF_6$ in EC/EMC (1/1)	2.8 – 4.3 V	1.0 C	2.5 mg cm^{-2}	70.3% @500	*J. Colloid Interface Sci.* **2023**[57]
$LiNi_{0.9}Co_{0.05}Mn_{0.05}O_2$	1.0 M $LiPF_6$ in EC/EMC (1/1)	2.8 – 4.3 V	0.5 C	N/A	93.3% @50	*Int. J. Electrochem. Sci.* **2023**[58]
$LiNi_{0.91}Co_{0.06}Mn_{0.03}O_2$	1.0 M $LiPF_6$ in EC/EMC/DMC (1/1/1)	3.0 – 4.3 V	0.5 C	15.5 mg cm^{-2}	82.6% @80	*Solid State Ion.* **2022**[59]
$Li_{1.08}Ni_{0.9}Mn_{0.1}O_2$	1.0 M $LiPF_6$ in EC/EMC (1/1)	2.7 – 4.6 V	0.1 C	4 mg cm^{-2}	96% @100	*Energy Storage Mater.* **2023**[60]
$LiNi_{0.9}Co_{0.04}Mn_{0.03}Al_{0.03}O_2$	N/A	2.8 – 4.5 V	0.5 C	N/A	91.8% @100	*Ceram. Int.* **2023**[61]

$LiNi_{0.91}Co_{0.06}Mn_{0.03}O_2$	1.0 M $LiPF_6$ in EC/EMC/DMC (1/1/1)	3.0 – 4.5 V	0.5 C	N/A	61.9% @100	*Int. J. Hydrog.* **2019**[62]
$LiNi_{0.9}Co_{0.05}Mn_{0.05}O_2$	1.2 M $LiPF_6$ in EC/EMC (3/7) with 2 wt.% VC additive	2.7 – 4.3 V	0.5 C	4 – 5 mg cm^{-2}	96% @100	*J. Power Sources* **2019**[63]
$LiNi_{0.9}Co_{0.05}Mn_{0.05}O_2$	1.0 M $LiPF_6$ in EC/EMC (3/7) with TMSFS additive	3.0 – 4.3 V	1.0 C	2 – 2.5 mg cm^{-2}	85.1% @200	*J. Power Sources* **2021**[64]
$LiNi_{0.95}Co_{0.03}Al_{0.01}Mg_{0.01}O_2$	1.15 M $LiPF_6$ in EC/DMC/EMC (1/2/2)	2.7 – 4.3 V	1.0 C	2 mg cm^{-2}	95.6% @100	*J. Power Sources* **2022**[65]
$LiNi_{0.925}Co_{0.03}Mn_{0.045}O_2$	1.0 M $LiPF_6$ in EC/EMC/DMC (1/1/1)	2.8 – 4.3 V	1.0 C	N/A	72.86% @100	*J. Power Sources* **2022**[66]
$LiNi_{0.91}Co_{0.04}Mn_{0.04}Al_{0.01}O_2$	1.2 M $LiPF_6$ in EC/EMC (3/7) with 2 wt.% VC additive	2.7 – 4.3 V	0.5 C	4 mg cm^{-2}	79.0% @100	*J. Power Sources* **2023**[67]
$LiNi_{0.9}Mn_{0.1}O_2$	1.0 M $LiPF_6$ in EC/EMC/DMC (1/1/1)	2.5 – 4.5 V	1.0 C	N/A	71.3% @100	*J. Alloys Compd.* **2019**[68]
$LiNi_{0.9}Co_{0.04}Mn_{0.03}Al_{0.03}O_2$	N/A	3.0 – 4.3 V	1.0 C	9.73 mg cm^{-2}	90.5% @100	*J. Alloys Compd.* **2023**[69]
$LiNi_{0.9}Co_{0.05}Mn_{0.05}O_2$	1.0 M $LiPF_6$ in EC/DEC (1/1)	2.7 – 4.3 V	1.0 C	N/A	90.2% @200	*J. Alloys Compd.* **2023**[70]
$Li(Ni_{0.9}Co_{0.1})_{0.97}Mg_{0.03}O_2$	1.2 M $LiPF_6$ in EC/EMC (3/7)	2.7 – 4.3 V	0.2 C	7.0 mg cm^{-2}	99.2% @100	*Chem. Eng. J.* **2021**[71]
$LiNi_{0.94}Co_{0.055}Mn_{0.005}O_2$	1.0 M $LiPF_6$ in EC/DMC (3/7)	2.8 – 4.3 V	1.0 C	5.33-5.85 mg cm^{-2}	89.6% @100	*Chem. Eng. J.* **2022**[72]
$LiNi_{0.9}Co_{0.05}Mn_{0.05}O_2$	1.0 M $LiPF_6$ in EC/EMC/EMC (1/1/1)	2.8 4.3 V	1.0 C	4 – 5 mg cm^{-2}	95.2% @100	*Chem. Eng. J.* **2023**[73]
$LiNi_{0.9}Co_{0.1}O_2$	1.0 M $LiPF_6$ in EC/DMC/EMC (1/1/1)	2.75 – 4.5 V	0.2 C	N/A	92.1% @100	*Chem. Eng. J.* **2023**[74]
$LiNi_{0.91}Co_{0.06}Mn_{0.03}O_2$	1.0 M $LiPF_6$ in EC/DMC/EMC (1/1/1)	3.0 – 4.3 V	0.5 C	14.5 mg cm^{-2}	87.2% @100	*Curr. Appl. Phys.* **2022**[75]
$LiNi_{0.98}Co_{0.02}O_2$	N/A	3.0 – 4.3 V	1.0 C	1.4 mg cm^{-2}	80.02% @200	*J. Electroanal. Chem.* **2023**[76]
$LiNi_{0.9}Co_{0.05}Mn_{0.05}O_{1.99}F_{0.01}$	1.0 M $LiPF_6$ in EC/DMC (1/1)	2.8 – 4.3 V	2.0 C	1 mg cm^{-2}	95.5% @100	*J. Energy Chem.* **2021**[77]
$LiNi_{0.9}Co_{0.055}Mn_{0.045}O_2$	1.0 M $LiPF_6$ in EC/EMC/DMC (1/1/1)	2.8 – 4.3 V	1.0 C	1.77 mg cm^{-2}	93% @50	*J. Energy Chem.* **2022**[78]
$LiNi_{0.9}Co_{0.05}Mn_{0.05}O_2$	1.0 M $LiPF_6$ in EC/DMC (1/1) with 5% FEC additive	2.8 – 4.3 V	0.5 C	N/A	93.9% @100	*J. Energy Chem.* **2022**[79]
$LiNi_{0.9}Co_{.1}O_2$	1.0 M $LiPF_6$ in EC/DMC/EMC (1/1/1)	2.8 – 4.3 V	0.2 C	N/A	97.9% @100	*Nano Energy* **2019**[80]
$LiNi_{0.9}Co_{0.05}Mn_{0.05}O_2$	1.0 M $LiPF_6$ in EC/DEC (1/1) with 2 wt.% MSTFA	3 – 4.3 V	0.25/0.5 C Ch./Disch.	15 mg cm^{-2}	85.9% @300	*Nano Energy* **2023**[81]
$LiNi_{0.95}Co_{0.04}Al_{0.01}O_2$	1.2 M $LiPF_6$ in EC/EMC (3/7) with 2 wt.% VC additive	2.7 – 4.3 V	0.5 C	4 mg cm^{-2}	90.3% @100	*Energy Storage Mater.* **2020**[82]
$LiNi_{0.94}Co_{0.03}Mn_{0.02}Al_{0.01}O_2$	1.2 M $LiPF_6$ in EC/EMC (3/7) with 2 wt.% VC additive	2.7 – 4.3 V	0.5 C	4 – 5 mg cm^{-2}	93.1% @100	*Energy Storage Mater.* **2023**[83]
$LiNi_{0.9}Co_{0.05}Mn_{0.05}O_2$	1.0 M $LiPF_6$ in EC/DMC/EMC (1/1/1)	2.7 – 4.5 V	0.5 C	5.1 mg cm^{-2}	85.0% @200	*Mater. Today Energy* **2023**[84]

$LiNi_{0.95}Mn_{0.05}O_2$	1.0 M $LiPF_6$ in EC/DMC/EMC (1/1/1) 0.3 wt.% LiBOB additive	2.7 – 4.3 V	1.0 C	2.5 mg cm^{-2}	84.4% @200	*eScience* **2022**[85]
$LiNi_{0.9}Co_{0.1}O_2$	1.0 M $LiPF_6$ in EC/EMC (3/7) with 2 wt.% VC additive	2.7 – 4.4 V	1.0 C	18.0 mg cm^{-2}	96.2% @100	*eScience* **2023**[86]
$LiNi_{0.901}Co_{0.051}Mn_{0.048}O_2$	1.2 M $LiPF_6$ in EC/EMC (3/7) with 2 wt.% VC additive	2.7 – 4.3 V	0.5 C	N/A	84.7% @100	*Small* **2018**[87]
$LiNi_{0.9}Al_{0.1}O_2$	1.0 M $LiPF_6$ in EC/DMC/EMC (1/1/1)	2.8 – 4.3 V	1.0 C	N/A	91.8% @400	*Nano Res.* **2023**[88]
$LiNi_{0.9}Co_{0.05}Mn_{0.05}O_2$	1.2 M $LiPF_6$ in EC/EMC (3/7) with 2 wt.% VC additive	2.7 – 4.3 V	0.5 C	4 – 5 mg cm^{-2}	80.5% @100	*J. Solid State Electrochem.* **2022**[89]
$LiNi_{0.95}Mn_{0.05}O_2$	1.0 M $LiPF_6$ in EC/DMC/EMC (1/1/1)	2.7 – 4.3 V	1.0 C	2.2 mg cm^{-2}	98.16% @100	*Nano Res.* **2022**[90]
$LiNi_{0.91}Co_{0.06}Mn_{0.03}O_2$	1.0 M $LiPF_6$ in FEC/DMC	N/A	1.0 C	10 mg cm^{-2}	77.16% @50	*Sci. Rep.* **2017**[91]
$LiNi_{0.9}Co_{0.1}O_2$	1.2 M $LiPF_6$ in EC/EMC (3/7) with 2 wt.% VC additive	2.7 – 4.5 V	1.0 C	N/A	96.8% @100	*Natl. Sci. Rev.* **2023**[92]
$LiNi_{0.9}Co_{0.05}Mn_{0.05}O_2$	1.2 M $LiPF_6$ in EC/EMC (3/7)	3.0 – 4.3 V	0.5 C	9 – 10 mg cm^{-2}	91.7% @80	*Int. J. Energy Res.* **2022**[93]
$LiNi_{0.9}Mn_{0.1}O_2$	1.2 M $LiPF_6$ in EC/EMC (3/7) with 2 wt.% VC additive	2.75 – 4.3 V	1.0 C	2.0 mg cm^{-2}	90.1% @100	*Battery Energy* **2022**[94]
$LiNi_{0.9}Mn_{0.1}O_2$	1.0 M $LiPF_6$ in EC/DMC/EMC (1/1/1)	2.8 – 4.3 V	0.5 C	N/A	95.6% @100	*Energy Fuels* **2023**[95]
$LiNi_{0.91}Co_{0.06}Mn_{0.03}O_2$	1.0 M $LiPF_6$ in EC/DMC/EMC (1/1/1)	3.0 – 4.3 V	0.5 C	15 mg cm^{-2}	82.4% @100	*Sci. Rep.* **2021**[96]
$LiNi_{0.9}Co_{0.1}O_2$	1.0 M $LiPF_6$ in EC/DMC/EMC (1/1/1)	2.8 – 4.3 V	1.0 C	2 mg cm^{-2}	76% @300	*Adv. Mater. Interfaces* **2021**[97]
$LiNi_{0.94}Co_{0.06}O_2$	1.2 M $LiPF_6$ in EC/EMC (3/7) with 2 wt.% VC additive	2.8 – 4.4 V	0.33 C	2 mAh cm^{-2}	94% @100	*Adv. Energy Mater.* **2021**[98]
$LiNi_{0.9}Mn_{0.05}Al_{0.05}O_2$	1.5 M $LiPF_6$ in EMC with 20 wt.% FEC and 1 wt.% LiTDI additive	2.5 – 4.4 V	1.0 C	10 mg cm^{-2}	~88% @100	*Adv. Energy Mater.* **2022**[99]
$LiNi_{0.9}Co_{0.07}Mg_{0.03}O_2$	1.15 M $LiPF_6$ in EC/DMC/EMC (1/2/2)	2.8 – 4.5 V	2.0 C	6.4 mg cm^{-2}	84.3% @300	*Chem. Sci.* **2019**[100]
$LiNi_{0.9}Co_{0.045}Mn_{0.045}Al_{0.01}O_2$	1.2 M $LiPF_6$ in EC/EMC (3/7) with 2 wt.% VC additive	2.7 – 4.4 V	1.0 C	N/A	96.7% @100	*J. Mater. Chem. A* **2023**[101]
$LiNi_{0.9}Co_{0.08}Al_{0.02}O_2$	1.0 M $LiPF_6$ in EC/DMC (1/1)	2.75 – 4.25 V	1.0 C	N/A	82.9% @100	*Rare Met.* **2021**[102]
$LiNi_{0.9}Co_{0.05}Mn_{0.05}O_2$	1.0 M $LiPF_6$ in EC/EMC (3/7) with 2 wt.% VC additive	2.8 – 4.4 V	0.33 C	10 mg cm^{-2}	89% @100	*Adv. Funct. Mater.* **2021**[103]
$LiNi_{0.94}Co_{0.06}O_2$	1.0 M $LiPF_6$ in EC/EMC (3/7) with 2 wt.% VC additive	2.8 – 4.4 V	0.33 C	1 mAh cm^{-2}	92% @100	*Chem. Mater.* **2020**[104]
$LiNi_{0.92}Co_{0.06}Al_{0.02}O_2$	1.0 M $LiPF_6$ in EC/EMC (3/7) with 2 wt.% VC additive	2.7 – 4.4 V	0.5 C	4 mg cm^{-2}	90% @200	*Chem. Mater.* **2018**[105]
$LiNi_{0.94}Co_{0.06}O_2$	1.0 M $LiPF_6$ in EC/EMC (3/7) with 2 wt.% VC additive	2.8 – 4.4 V	0.33 C	5 mg cm^{-2}	85% @200	*Chem. Mater.* **2019**[106]
$LiNi_{0.94}Co_{0.06}O_2$	1.0 M $LiPF_6$ in EC/EMC (3/7) with 2 wt.% VC	2.8 – 4.4 V	0.33 C	8 mg cm^{-2}	87% @200	*Chem. Mater.* **2020**[107]

	additive					
$LiNi_{0.9}Co_{0.05}Mn_{0.05}O_2$	1.0 M $LiPF_6$ in EC/EMC (3/7) with 0.3% TBDB additive	3.0 – 4.3 V	1.0 C	1.5 mg cm^{-2}	84.3% @200	*ACS Appl. Energy Mater.* **2021**[108]
$LiNi_{0.9}Mn_{0.05}Al_{0.05}O_2$	1.2 M $LiPF_6$ in EC/EMC (3/7)	2.8 – 4.4 V	0.33 C	1 mAh cm^{-2}	80% @100	*ACS Appl. Energy Mater.* **2022**[109]
$LiNi_{0.95}Co_{0.04}Al_{0.01}O_2$	1.2 M $LiPF_6$ in EC/EMC (3/7) with 2 wt.% VC additive	2.7 – 4.3 V	0.5 C	N/A	81.6% @100	*ACS Energy Lett.* **2019**[110]
$LiNi_{0.9}Co_{0.05}Mn_{0.05}O_2$	1.0 M $LiPF_6$ in EC/EMC (3/7) with 0.5 wt.% TDSTCN additive	2.7 – 4.25 V	1.0 C	5.5 mg cm^{-2}	93.63% @100	*Adv. Funct. Mater.* **2023**[111]
$LiNi_{0.9}Co_{0.1}O_2$	1.0 M $LiPF_6$ in EC/EMC (3/7) with 2 wt.% VC additive	2.7 – 4.3 V	0.2 C	1.7 – 2.5 mg cm^{-2}	68.3% @200	*Chem. Eng. Sci.* **2020**[112]
$LiNi_{0.9}Mn_{0.1}O_2$	1.2 M $LiPF_6$ in EC/EMC (3/7)	3.0 – 4.3 V	0.3 C	N/A	84% @103	*Electrochim. Acta* **2021**[113]
$LiNi_{0.9}Co_{0.05}Mn_{0.05}O_2$	1.0 M $LiPF_6$ in EC/DMC/EMC (1/1/1)	2.8 – 4.3 V	0.5 C	2 – 3 mg cm^{-2}	90% @100	*Electrochim. Acta* **2022**[114]
$LiNi_{0.95}Mn_{0.05}O_2$	1.0 M $LiPF_6$ in EC/DMC/EMC (1/1/1)	2.75 – 4.3 V	1.0 C	N/A	89.93% @100	*Electrochim. Acta* **2022**[115]
$LiNi_{0.9}Co_{0.04}Mn_{0.06}O_2$	1.0 M $LiPF_6$ in EC/DMC (1/1)	2.5 – 4.3 V	0.5 C	N/A	93.3% @100	*Ceram. Int.* **2022**[116]
$LiNi_{0.9}Mn_{0.1}O_2$	1.0 M $LiPF_6$ in EC/DMC/EMC (1/1/1)	2.75 – 4.3 V	1.0 C	3.5 mg cm^{-2}	87.5% @200	*J. Alloy Compd.* **2021**[117]
$LiNi_{0.9}Mn_{0.1}O_2$	1.0 M $LiPF_6$ in EC/DMC/EMC (1/1/1)	2.7 – 4.3 V	5.0 C	3.1 mg cm^{-2}	86.4% @100	*J. Alloy Compd.* **2023**[118]
$LiNi_{0.9}Co_{0.08}Mn_{0.02}O_2$	1.0 M $LiPF_6$ in EC/DMC/EMC	2.8 – 4.3 V	0.5 C	N/A	93.4% @200	*Energy Storage Mater.* **2020**[119]

Supplementary Table 4. Structural parameters of EEC-Ni90 as a function of SoC obtained by in-situ EXAFS fitting results

SoC	Shell	CN	σ^2 (Å^2)	Err(σ^2)	R (Å)	Err(R)	R-factor
0	Ni-O1	6	0.01055	0.00096294	1.94676	0.00905626	0.005035
	Ni-TM	6	0.00439	0.00025054	2.87971	0.00598293	
0.09	Ni-O1	6	0.01064	0.00107058	1.94587	0.01006099	0.0063660
	Ni-TM	6	0.00454	0.00028249	2.87868	0.00668835	
0.19	Ni-O1	6	0.01058	0.00107433	1.94908	0.01007830	0.0063132
	Ni-TM	6	0.00444	0.00027961	2.88020	0.00665765	
0.28	Ni-O1	6	0.01056	0.00108372	1.94687	0.01014195	0.0065298
	Ni-TM	6	0.00447	0.00028614	2.87761	0.00673899	
0.37	Ni-O1	6	0.01027	0.00113288	1.94500	0.01093077	0.0073779
	Ni-TM	6	0.00444	0.00030771	2.84290	0.00746214	
0.47	Ni-O1	6	0.01032	0.00115080	1.94170	0.01106157	0.0075836
	Ni-TM	6	0.00447	0.00031387	2.87423	0.00758314	
0.52	Ni-O1	6	0.01035	0.00117879	1.94437	0.01111178	0.0080949
	Ni-TM	6	0.00450	0.00031945	2.87586	0.00751449	
0.56	Ni-O1	6	0.01060	0.00121436	1.94309	0.01138064	0.0081857
	Ni-TM	6	0.00450	0.00032086	2.87507	0.00760062	
0.63	Ni-O1	6	0.01015	0.00117154	1.93112	0.01097012	0.0083358
	Ni-TM	6	0.00450	0.00032484	2.86878	0.00755965	
0.7	Ni-O1	6	0.00989	0.00108498	1.92217	0.01061170	0.0076899
	Ni-TM	6	0.00471	0.00032303	2.86324	0.00760442	
0.8	Ni-O1	6	0.00797	0.00122424	1.89971	0.01183159	0.0145147
	Ni-TM	6	0.00460	0.00044757	2.84845	0.00948100	
0.89	Ni-O1	6	0.00542	0.00093444	1.88187	0.00953000	0.0125684
	Ni-TM	6	0.00411	0.00043800	2.82969	0.00867930	
0.94	Ni-O1	6	0.00472	0.00089728	1.87883	0.00925308	0.0124013
	Ni-TM	6	0.00374	0.00043720	2.82506	0.00865523	

Supplementary Table 5. Structural parameters obtained by EXAFS fitting data for EEC-Ni90 before and after cycling at 0.5C and 55 ^{o}C for 150 cycles

Samples	Shell	CN	σ^2 (Å^2)	R (Å)	Err (R)	R-factor
EEC-Ni90 pristine	Ni-O1	6	0.01235	1.94206	0.00936	0.0067
	Ni-TM	6	0.00661	2.87183	0.00605	
	Ni-O2	6	0.03749	3.21671	0.09597	
EEC-Ni90-Disch. 2.5 V 150th cycle	Ni-O1	6	0.00905	1.93988	0.00895	0.0081
	Ni-TM	6	0.00560	2.87246	0.00661	
	Ni-O2	6	0.00383	3.29150	0.002531	

Supplementary Table 6. Thermal stability comparison of delithiated Ni90, ZrO_2-Ni90, and EEC-Ni90 cathode. L, S and R represent layered, spinel and rock-salt, respectively.

Cathode	SoC	Peak Temp_L-S	Heat Generation_L-S	Peak Temp_S-R	Heat Generation_S-R
Ni90	80%	219.7 °C	-90.52 J g^{-1}	305.1 °C	-666.19 J g^{-1}
ZrO_2-Ni90	80%	220.65 °C	-77.00 J g^{-1}	324.07 °C	-230.75 J g^{-1}
EEC-Ni90	80%	222.87 °C	-73.09 J g^{-1}	366.53 °C	-84.72 J g^{-1}

Supplementary References

1. Biesinger, M. C. Accessing the robustness of adventitious carbon for charge referencing (correction) purposes in XPS analysis: Insights from a multi-user facility data review. *Appl. Surface Sci.* **597**, 153681, (2022).

2. Jiao, S. et al. Stable cycling of high-voltage lithium metal batteries in ether electrolytes. *Nat. Energy* **3**, 739-746 (2018).

3. Wu, F. et al. Dual-anion ionic liquid electrolyte enables stable Ni-rich cathodes in lithium-metal batteries. *Joule* **5**, 2177-2194 (2021).

4. Zhao, W. et al. High Voltage Operation of Ni-Rich NMC Cathodes Enabled by Stable Electrode/Electrolyte Interphases. *Adv. Energy Mater.* **8**, 1800297 (2018).

5. Wu, J. et al. A synergistic exploitation to produce high-voltage quasi-solid-state lithium metal batteries. *Nat. Commun*. **12**, 5746 (2021).

6. Huang, Z., Meng, J., Xie, M., Shen, Y. & Huang, Y. A pretreatment method to form high-quality LiF-enriched solid-electrolyte interfaces for Li anode protection in Li–O2 batteries. *J. Mater. Chem. A* **8**, 14198-14204 (2020).

7. Katzbaer, R. R., dos Santos Vieira, F. M., Dabo, I., Mao, Z. & Schaak, R. E. Band Gap Narrowing in a High-Entropy Spinel Oxide Semiconductor for Enhanced Oxygen Evolution Catalysis. *J. Am. Chem. Soc*. **145**, 6753-6761 (2023).

8. Sarkar, A. et al. High entropy oxides for reversible energy storage. *Nat. Commun.* **9**, 3400 (2018).

9. Xiao, Y., Miara, L. J., Wang, Y. & Ceder, G. Computational Screening of Cathode Coatings for Solid-State Batteries. *Joule* **3**, 1252-1275 (2019).

10. Kim, U.-H. et al. Heuristic solution for achieving long-term cycle stability for Ni-rich layered cathodes at full depth of discharge. *Nat. Energy* **5**, 860-869 (2020).

11. Park, G.-T. et al. Introducing high-valence elements into cobalt-free layered cathodes for practical lithium-ion batteries. *Nat. Energy* **7**, 946-954 (2022).

12. Sun, H. H. et al. Transition metal-doped Ni-rich layered cathode materials for durable Li-ion batteries. *Nat. Commun.* **12**, 6552 (2021).

13. Yu, H. et al. Surface enrichment and diffusion enabling gradient-doping and coating of Ni-rich cathode toward Li-ion batteries. *Nat. Commun.* **12**, 4564 (2021).

14. Sheng, H. et al. An Air-Stable High-Nickel Cathode with Reinforced Electrochemical Performance Enabled by Convertible Amorphous Li_2CO_3 Modification. *Adv. Mater.* **34**, 2108947 (2022).

15. Park, N.-Y., Cho, G., Kim, S.-B. & Sun, Y.-K. Multifunctional Doping Strategy to Develop High-Performance Ni-Rich Cathode Material. *Adv. Energy Mater*. **13**, 2204291 (2023).

16. Qiu, L. et al. Structural Reconstruction Driven by Oxygen Vacancies in Layered Ni-Rich Cathodes. *Adv. Energy Mater*. **12**, 2200022 (2022).

17. Park, N.-Y., Ryu, H.-H., Park, G.-T., Noh, T.-C. & Sun, Y.-K. Optimized Ni-Rich NCMA Cathode for Electric Vehicle Batteries. *Adv. Energy Mater*. **11**, 2003767 (2021).
18. Ryu, H.-H. et al. New Class of Ni-Rich Cathode Materials $Li[Ni_xCo_yB_{1-x-y}]O_2$ for Next Lithium Batteries. *Adv. Energy Mater.* **10**, 2000495 (2020).
19. Ryu, H.-H. et al. $Li[Ni_{0.9}Co_{0.09}W_{0.01}]O_2$: A New Type of Layered Oxide Cathode with High Cycling Stability. *Adv. Energy Mater*. **9**, 1902698 (2019).
20. Park, K.-J. et al. Improved Cycling Stability of $Li[Ni_{0.90}Co_{0.05}Mn_{0.05}]O_2$ Through Microstructure Modification by Boron Doping for Li-Ion Batteries. *Adv. Energy Mater*. **8**, 1801202 (2018).
21. Aishova, A., Park, G.-T., Yoon, C. S. & Sun, Y.-K. Cobalt-Free High-Capacity Ni-Rich Layered $Li[Ni_{0.9}Mn_{0.1}]O_2$ Cathode. *Adv. Energy Mater.* **10**, 1903179 (2020).
22. Kim, U.-H. et al. Microstructure-Controlled Ni-Rich Cathode Material by Microscale Compositional Partition for Next-Generation Electric Vehicles. Adv. Energy Mater. **9**, 1803902 (2019).
23. Jung, C.-H. et al. New Insight into Microstructure Engineering of Ni-Rich Layered Oxide Cathode for High Performance Lithium Ion Batteries. *Adv. Funct. Mater*. **31**, 2010095 (2021).
24. Sun, Y. et al. One-Step Calcination Synthesis of Bulk-Doped Surface-Modified Ni-Rich Cathodes with Superlattice for Long-Cycling Li-Ion Batteries. *Angew. Chem. Int. Ed*. **62**, e202300962 (2023).
25. Xin, F. et al. Electrochemical Characterization and Microstructure Evolution of Ni-Rich Layered Cathode Materials by Niobium Coating/Substitution. *Chem. Mater*. **34**, 7858-7866 (2022).
26. Sun, H.-H. & Manthiram, A. Impact of Microcrack Generation and Surface Degradation on a Nickel-Rich Layered $Li[Ni_{0.9}Co_{0.05}Mn_{0.05}]O_2$ Cathode for Lithium-Ion Batteries. *Chem. Mater.* **29**, 8486-8493 (2017).
27. Ryu, H.-H., Park, K.-J., Yoon, C. S. & Sun, Y.-K. Capacity Fading of Ni-Rich $Li[Ni_xCo_yMn_{1-x-y}]O_2$ ($0.6 \leq x \leq 0.95$) Cathodes for High-Energy-Density Lithium-Ion Batteries: Bulk or Surface Degradation? *Chem. Mater*. **30**, 1155-1163 (2018).
28. Li, H. et al. An Unavoidable Challenge for Ni-Rich Positive Electrode Materials for Lithium-Ion Batteries. *Chem. Mater*. **31**, 7574-7583 (2019).
29. Abebe, E. B., Yang, C.-C., Wu, S.-H., Chien, W.-C. & Li, Y.-J. J. Effect of Li Excess on Electrochemical Performance of Ni-Rich $LiNi_{0.9}Co_{0.05}Mn_{0.05}O_2$ Cathode Materials for Li-Ion Batteries. *ACS Appl. Energy Mater*. **4**, 14295-14308 (2021).
30. Su, Y. et al. Riveting Dislocation Motion: The Inspiring Role of Oxygen Vacancies in the Structural Stability of Ni-Rich Cathode Materials. *ACS Appl. Mater. Interfaces* **12**, 37208-37217 (2020).
31. Zou, Y. et al. Enhanced Cycle Life and Rate Capability of Single-Crystal, Ni-Rich $LiNi_{0.9}Co_{0.05}Mn_{0.05}O_2$ Enabled by 1,2,4-1H-Triazole Additive. *ACS Appl. Mater.*

Interfaces **13**, 16427-16436 (2021).
32. Wu, F. et al. A Universal Method for Enhancing the Structural Stability of Ni-Rich Cathodes Via the Synergistic Effect of Dual-Element Cosubstitution. *ACS Appl. Mater. Interfaces* **13**, 24925-24936 (2021).
33. Zhu, C. et al. Synergistic Effect of Microstructure Engineering and Local Crystal Structure Tuning to Improve the Cycling Stability of Ni-Rich Cathodes. *ACS Appl. Mater. Interfaces* **13**, 48720-48729 (2021).
34. Hu, Y. et al. Effective and Low-Cost In Situ Surface Engineering Strategy to Enhance the Interface Stability of an Ultrahigh Ni-Rich NCMA Cathode. *ACS Appl. Mater. Interfaces* **14**, 51835-51845 (2022).
35. Min, K. et al. High-Performance and Industrially Feasible Ni-Rich Layered Cathode Materials by Integrating Coherent Interphase. *ACS Appl. Mater. Interfaces* **10**, 20599-20610 (2018).
36. Kim, J.-H., Ryu, H.-H., Kim, S. J., Yoon, C. S. & Sun, Y.-K. Degradation Mechanism of Highly Ni-Rich $Li[Ni_xCo_yMn_{1-x-y}]O_2$ Cathodes with x > 0.9. *ACS Appl. Mater. Interfaces* **11**, 30936-30942 (2019).
37. Ryu, H.-H. et al. Microstrain Alleviation in High-Energy Ni-Rich NCMA Cathode for Long Battery Life. *ACS Energy Lett*. **6**, 216-223 (2021).
38. Qian, R. et al. Enhanced Surface Chemical and Structural Stability of Ni-Rich Cathode Materials by Synchronous Lithium-Ion Conductor Coating for Lithium-Ion Batteries. *ACS Appl. Mater. Interfaces* **12**, 13813-13823 (2020).
39. Ryu, H.-H. et al. Capacity Fading Mechanisms in Ni-Rich Single-Crystal NCM Cathodes. *ACS Energy Lett.* **6**, 2726-2734 (2021).
40. Han, G.-M., Kim, Y.-S., Ryu, H.-H., Sun, Y.-K. & Yoon, C. S. Structural Stability of Single-Crystalline Ni-Rich Layered Cathode upon Delithiation. *ACS Energy Lett*. **7**, 2919-2926 (2022).
41. Ryu, H.-H., Lee, S.-B., Yoon, C. S. & Sun, Y.-K. Morphology-Dependent Battery Performance of Ni-Rich Layered Cathodes: Single-Crystal versus Refined Polycrystal. *ACS Energy Lett*. **7**, 3072-3079 (2022).
42. Sun, H. H., Dolocan, A., Weeks, J. A., Heller, A. & Mullins, C. B. Stabilization of a Highly Ni-Rich Layered Oxide Cathode through Flower-Petal Grain Arrays. *ACS Nano* **14**, 17142-17150 (2020).
43. Dai, P. et al. Single-Crystal Ni-Rich Layered $LiNi_{0.9}Mn_{0.1}O_2$ Enables Superior Performance of Co-Free Cathodes for Lithium-Ion Batteries. *ACS Sustain. Chem. Eng.* **10**, 4381-4390 (2022).
44. Tan, Z. et al. Lattice Engineering to Refine Particles and Strengthen Bonds of the $LiNi_{0.9}Co_{0.05}Mn_{0.05}O_2$ Cathode toward Efficient Lithium Ion Storage. *ACS Sustain. Chem. Eng.* **10**, 3532-3545 (2022).
45. Ryu, H.-H., Lim, H.-W., Kang, G.-C., Park, N.-Y. & Sun, Y.-K. Long-Lasting Ni-

Rich NCMA Cathodes via Simultaneous Microstructural Refinement and Surface Modification. *ACS Energy Lett*. **8**, 1354-1361 (2023).
46. Zhou, P. et al. Stable layered Ni-rich $LiNi_{0.9}Co_{0.07}Al_{0.03}O_2$ microspheres assembled with nanoparticles as high-performance cathode materials for lithium-ion batteries. *J. Mater. Chem. A* **5**, 2724-2731 (2017).
47. Kim, J.-H., Park, K.-J., Kim, S. J., Yoon, C. S. & Sun, Y.-K. A method of increasing the energy density of layered Ni-rich $Li[Ni_{1-2x}Co_xMn_x]O_2$ cathodes (x = 0.05, 0.1, 0.2). *J. Mater. Chem. A* **7**, 2694-2701 (2019).
48. Su, Y. et al. Roles of Fast-Ion Conductor $LiTaO_3$ Modifying Ni-rich Cathode Material for Li-Ion Batteries. *ChemSusChem* **14**, 1955-1961 (2021).
49. Zhang, C. et al. Restraining the polarization increase of Ni-rich and low-Co cathodes upon cycling by Al-doping. *J. Mater. Chem. A* **8**, 6893-6901 (2020).
50. Park, G.-T. et al. Ultrafine-grained Ni-rich layered cathode for advanced Li-ion batteries. *Energy Environ. Sci*. **14**, 6616-6626 (2021).
51. Susai, F. A. et al. Stabilizing Ni-rich high energy cathodes for advanced lithium-ion batteries: the case of $LiNi_{0.9}Co_{0.1}O_2$. *J. Mater. Chem. A* **11**, 12958-12972 (2023).
52. Luo, Z. et al. Effect of Mg and Zr co-doping on the Co-less Ni-rich cathode materials for advanced lithium-ion batteries. *J. Energy Storage* **68**, 107777 (2023).
53. Iqbal, A. & Li, D. Systematic study of the effect of calcination temperature and Li/M molar ratio on high performance Ni-rich layered $LiNi_{0.9}Co_{0.1}O_2$ cathode materials. *Chem. Phys. Lett.* **720**, 97-106 (2019).
54. Xia, Y. et al. Spinel $LiNi_{0.5}Mn_{1.5}O_4$ shell enables Ni-rich layered oxide cathode with improved cycling stability and rate capability for high-energy lithium-ion batteries. *Electrochim. Acta* **418**, 140352 (2022).
55. Sattar, T., Lee, S.-H., Sim, S.-J., Jin, B.-S. & Kim, H.-S. Understanding the combined effect of Ca doping and phosphate coating on Ni-rich $LiNi_{0.91}Co_{0.06}Mn_{0.03}O_2$ cathode material for Li-ion batteries. *Electrochim. Acta* **399**, 139417 (2021).
56. Tao, Z., Liu, G., Li, S., Yao, M. & Zhang, Y. Rational structure of rod-like single crystal $LiNi_{0.9}Co_{0.05}Mn_{0.04}Al_{0.01}O_2$ cathode for superior-stable lithium-ion battery. *Electrochim. Acta* **444**, 141975 (2023).
57. Jeyakumar, J. et al. Preparation of long-term cycling stable ni-rich concentration–gradient NCMA cathode materials for li-ion batteries. *J. Colloid Interface Sci*. **639**, 145-159 (2023).
58. Wu, Y.-L., Lan, C.-C., Liu, M.-H. & Lu, C.-J. Improving electrochemical performance of $LiNi_{0.9}Co_{0.05}Mn_{0.05}O_2$ cathode material by coating with nano-$LiNbO_3$ layer. *Int. J. Electrochem. Sci.* **18**, 100278 (2023).
59. Sattar, T., Sim, S.-J., Lee, S.-H., Jin, B.-S. & Kim, H.-S. Unveiling the impact of Mg doping and in-situ Li reactive coating on the Ni-rich cathode material for LIBs. *Solid State Ion*. **378**, 115886 (2022).

60. Jing, Z. et al. Architecting "Li-rich Ni-rich" core-shell layered cathodes for high-energy Li-ion batteries. *Energy Storage Mater.* **59**, 102775 (2023).
61. Yang, J., Gao, D., Zhang, D. & Chang, C. Suppressing the H2–H3 phase transition of $LiNi_{0.90}Co_{0.04}Mn_{0.03}Al_{0.03}O_2$ cathodes via Ta doping towards improved electrochemical performance upon 4.5V. *Cera. Int.* **49**, 22294-22303 (2023).
62. Lee, S.-H., Lee, S., Jin, B.-S. & Kim, H.-S. Preparation and electrochemical performances of Ni-rich $LiNi_{0.91}Co_{0.06}Mn_{0.03}O_2$ cathode for high-energy LIBs. *Int. J. Hydrog. Energy* **44**, 13684-13689 (2019).
63. Park, G.-T., Ryu, H.-H., Park, N.-Y., Yoon, C. S. & Sun, Y.-K. Tungsten doping for stabilization of $Li[Ni_{0.90}Co_{0.05}Mn_{0.05}]O_2$ cathode for Li-ion battery at high voltage. *J. Power Sources* **442**, 227242 (2019).
64. Jiao, T. et al. A novel trimethylsilyl 2-(fluorosulfonyl)difluoroacetate additive for stabilizing the Ni-rich $LiNi_{0.9}Co_{0.05}Mn_{0.05}O_2$/electrolyte interface. *J. Power Sources* **515**, 230618 (2021).
65. Zhang, Y. et al. Gradient doping Mg and Al to stabilize Ni-rich cathode materials for rechargeable lithium-ion batteries. *J. Power Sources* **535**, 231445 (2022).
66. Luo, Z. et al. Enhancing the electrochemical performance of Co-less Ni-rich $LiNi_{0.925}Co_{0.03}Mn_{0.045}O_2$ cathode material via Co-modification with $Li_2B_4O_7$ coating and B^{3+} doping. *J. Power Sources* **548**, 232092 (2022).
67. Kim, U.-H., Lee, S.-B., Ryu, J.-H., Yoon, C. S. & Sun, Y.-K. Optimization of Ni-rich $Li[Ni_{0.92-x}Co_{0.04}Mn_{0.04}Al_x]O_2$ cathodes for high energy density lithium-ion batteries. *J. Power Sources* **564**, 232850 (2023).
68. Zhang, J. T. et al. Controllable formation of lithium carbonate surface phase during synthesis of nickel-rich $LiNi_{0.9}Mn_{0.1}O_2$ in air and its protection role in electrochemical reaction. *J. Alloys Compd.* **771**, 42-50 (2019).
69. Ding, H. et al. Enhanced lithium storage capability of Ni-rich $LiNi_{0.9}CoxMn_{0.1-x}O_2(0 \leq x \leq 0.1)$ cathode by co-operation of Al-doping and V-coating. *J. Alloys Compd.* **946**, 169428 (2023).
70. Abebe, E. B., Yang, C.-C., Wu, S.-H., Chien, W.-C. & Li, Y.-J. J. Surface modification with Li_3PO_4 enhances the electrochemical performance of $LiNi_{0.9}Co_{0.05}Mn_{0.05}O_2$ cathode materials for Li-Ion batteries. *J. Alloys Compd.* **947**, 169455 (2023).
71. Yu, H. et al. Bulk Mg-doping and surface polypyrrole-coating enable high-rate and long-life for Ni-rich layered cathodes. *Chem. Eng. J.* **412**, 128625, (2021).
72. Guo, Z. et al. Protective and ion conductive: High-Rate Ni-Rich cathode with enhanced cyclic stability via One-Step bifunctional dual-layer coating. *Chem. Eng. J.* **431**, 134031 (2022).
73. Yao, M., Tao, Z., Liu, G., Li, S. & Zhang, Y. A novel calcination method towards layered Ni-rich cathode with enhanced electrochemical performances and regulated

oxygen vacancies. *Chem. Eng. J.* **473**, 145090 (2023).
74. Liu, N. et al. Phase behavior tuning enable high-safety and crack-free Ni-rich layered cathode for lithium-ion battery. *Chem. Eng. J.* **472**, 145113 (2023).
75. Sattar, T., Sim, S.-J., Jin, B.-S. & Kim, H.-S. Improving the cycle stability and rate performance of $LiNi_{0.91}Co_{0.06}Mn_{0.03}O_2$ Ni-rich cathode material by La_2O_3 coating for Lithium-ion batteries. *Curr. Appl. Phys*. **36**, 176-182 (2022).
76. Ji, F. et al. Significance of Al doping for excellent electrochemical performance of $LiNi_{0.98}Co_{0.02}O_2$ cathode materials. *J. Electroanal. Chem.* **940**, 117483 (2023).
77. Qiu, Q.-Q. et al. Suppressing irreversible phase transition and enhancing electrochemical performance of Ni-rich layered cathode $LiNi_{0.9}Co_{0.05}Mn_{0.05}O_2$ by fluorine substitution. *J. Energy Chem*. **61**, 574-581 (2021).
78. Wang, J. et al. Grain size regulation for balancing cycle performance and rate capability of $LiNi_{0.9}Co_{0.055}Mn_{0.045}O_2$ single crystal nickel-rich cathode materials. *J. Energy Chem.* **65**, 681-687 (2022).
79. Tan, Z. et al. A novelty strategy induced pinning effect and defect structure in Ni-rich layered cathodes towards boosting its electrochemical performance. *J. Energy Chem.* **72**, 570-580 (2022).
80. Wu, F. et al. Improving the reversibility of the H2-H3 phase transitions for layered Ni-rich oxide cathode towards retarded structural transition and enhanced cycle stability. *Nano Energy* **59**, 50-57 (2019).
81. Peng, Q. et al. Developing multifunctional amide additive by rational molecular design for high-performance Li metal batteries. *Nano Energy* **113**, 108547 (2023).
82. Kim, U.-H. et al. High-Energy W-Doped $Li[Ni_{0.95}Co_{0.04}Al_{0.01}]O_2$ Cathodes for Next-Generation Electric Vehicles. *Energy Storage Mater*. **33**, 399-407 (2020).
83. Ryu, H.-H., Lim, H.-W., Lee, S. G. & Sun, Y.-K. Optimization of molybdenum-doped Ni-rich layered cathodes for long-term cycling. *Energy Storage Mater*. **59**, 102771 (2023).
84. Xia, Y. et al. Binary-compositional core-shell structure Ni-rich cathode material with radially oriented primary particles in shell for long cycling lifespan lithium-ion batteries. *Mater. Today Energy* **34**, 101292 (2023).
85. Ni, L. et al. Crack-free single-crystalline Co-free Ni-rich $LiNi_{0.95}Mn_{0.05}O_2$ layered cathode. *eScience* **2**, 116-124 (2022).
86. Guo, W. et al. In situ surface engineering enables high interface stability and rapid reaction kinetics for Ni-rich cathodes. *eScience* **3**, 100082 (2023).
87. Ryu, H.-H., Park, G.-T., Yoon, C. S. & Sun, Y.-K. Microstructural Degradation of Ni-Rich $Li[Ni_xCo_yMn_{1-x-y}]O_2$ Cathodes During Accelerated Calendar Aging. *Small* **14**, 1803179 (2018).
88. Liu, L. et al. Dual-site lattice co-doping strategy regulated crystal-structure and microstructure for enhanced cycling stability of Co-free Ni-rich layered cathode. *Nano*

Res. **16**, 9250-9258 (2023).
89. Ryu, H.-H., Lee, S.-B. & Sun, Y.-K. Promoting grain growth in Ni-rich single-crystal cathodes for high-performance lithium-ion batteries through Ce doping. *J. Solid State Electrochem.* **26**, 2097-2105 (2022).
90. Wang, C. et al. Unveiling the impact of residual Li conversion and cation ordering on electrochemical performance of Co-free Ni-rich cathodes. *Nano Res.* **15**, 9038-9046 (2022).
91. Min, K. et al. Improved electrochemical properties of $LiNi_{0.91}Co_{0.06}Mn_{0.03}O_2$ cathode material via Li-reactive coating with metal phosphates. *Sci. Rep*. **7**, 7151 (2017).
92. Yu, H. et al. Restraining the escape of lattice oxygen enables superior cyclic performance towards high-voltage Ni-rich cathodes. *Natl. Sci. Rev*. **10** (2022).
93. Jeong, S. et al. The enhancement of cyclability of Ni-rich $LiNi_{0.9}Co_{0.05-x}Mn_{0.05}Zn_x$ cathode materials by the substitution of Zn for Co. *Int. J. Energy Res*. **46**, 19177-19189 (2022).
94. Yang, Z., Wang, Z., Zhu, Y., Jiang, H. & Li, C. Enhancing surface-to-bulk stability of layered Co-free Ni-rich cathodes for long-life Li-ion batteries. *Battery Energy* **2**, 20220048 (2023).
95. Hu, C. et al. Structural Reinforcement through High-Valence Nb Doping to Boost the Cycling Stability of Co-Free and Ni-Rich $LiNi_{0.9}Mn_{0.1}O_2$ Cathode Materials. *Energy Fuels* **37**, 8005-8013 (2023).
96. Sattar, T., Sim, S.-J., Jin, B.-S. & Kim, H.-S. Dual function Li-reactive coating from residual lithium on Ni-rich NCM cathode material for Lithium-ion batteries. *Sci. Rep.* **11**, 18590 (2021).
97. Tan, X. et al. Direct Elimination of Detrimental Surface Phases Parasitic to $LiNi_xCo_{1-x}O_2$ (x = 0.8 and 0.9) with Unique 3D Porous Structures during Synthesis. *Adv. Mater. Interfaces* **8**, 2100392 (2021).
98. Cui, Z., Xie, Q. & Manthiram, A. A Cobalt- and Manganese-Free High-Nickel Layered Oxide Cathode for Long-Life, Safer Lithium-Ion Batteries. *Adv. Energy Mater*. **11**, 2102421 (2021).
99. Pan, R., Cui, Z., Yi, M., Xie, Q. & Manthiram, A. Ethylene Carbonate-Free Electrolytes for Stable, Safer High-Nickel Lithium-Ion Batteries. *Adv. Energy Mater.* **12**, 2103806 (2022).
100. Li, H. et al. Stabilizing nickel-rich layered oxide cathodes by magnesium doping for rechargeable lithium-ion batteries. *Chem. Sci*. **10**, 1374-1379 (2019).
101. Wei, W., Wang, Z., Yao, L., Jiang, H. & Li, C. Stabilizing lattice oxygen and interface chemistry of Ni-rich and Co-poor cathodes for high-energy lithium-ion batteries. *J. Mater. Chem. A* **11**, 2979-2984 (2023).
102. Li, W.-W., Zhang, X.-J., Si, J.-J., Yang, J. & Sun, X.-Y. TiO_2-coated $LiNi_{0.9}Co_{0.08}Al_{0.02}O_2$ cathode materials with enhanced cycle performance for Li-ion

batteries. *Rare Met*. **40**, 1719-1726 (2021).
103. Langdon, J. & Manthiram, A. Crossover Effects in Batteries with High-Nickel Cathodes and Lithium-Metal Anodes. *Adv. Funct. Mater*. **31**, 2010267 (2021).
104. Xie, Q. & Manthiram, A. Long-Life, Ultrahigh-Nickel Cathodes with Excellent Air Storage Stability for High-Energy Density Lithium-Based Batteries. *Chem. Mater*. **32**, 7413-7424 (2020).
105. Li, J. et al. Facilitating the Operation of Lithium-Ion Cells with High-Nickel Layered Oxide Cathodes with a Small Dose of Aluminum. *Chem. Mater*. **30**, 3101-3109 (2018).
106. Xie, Q., Li, W., Dolocan, A. & Manthiram, A. Insights into Boron-Based Polyanion-Tuned High-Nickel Cathodes for High-Energy-Density Lithium-Ion Batteries. *Chem. Mater*. **31**, 8886-8897 (2019).
107. Li, J., Chang, C.-H. & Manthiram, A. Toward Long-Life, Ultrahigh-Nickel Layered Oxide Cathodes for Lithium-Ion Batteries: Optimizing the Interphase Chemistry with a Dual-Functional Polymer. *Chem. Mater*. **32**, 759-768 (2020).
108. Zou, Y. et al. Enhanced Interfacial Stability of a $LiNi_{0.9}Co_{0.05}Mn_{0.05}O_2$ Cathode by a Diboron Additive. *ACS Appl. Energy Mater*. **4**, 11051-11061 (2021).
109. Brow, R. et al. Mechanical Pulverization of Co-Free Nickel-Rich Cathodes for Improved High-Voltage Cycling of Lithium-Ion Batteries. *ACS Appl. Energy Mater*. **5**, 6996-7005 (2022).
110. Nam, G. W. et al. Capacity Fading of Ni-Rich NCA Cathodes: Effect of Microcracking Extent. *ACS Energy Lett.* **4**, 2995-3001 (2019).
111. Ren, Z. et al. Delicately Designed Cyano-Siloxane as Multifunctional Additive Enabling High Voltage $LiNi_{0.9}Co_{0.05}Mn_{0.05}O_2$/Graphite Full Cell with Long Cycle Life at 50 °C. *Adv. Funct. Mater*. **33**, 2302411 (2023).
112. Zhu, H. et al. High-efficiency Mo doping stabilized $LiNi_{0.9}Co_{0.1}O_2$ cathode materials for rapid charging and long-life Li-ion batteries. *Chem. Eng. Sci*. **217**, 115518 (2020).
113. Aryal, S., Durham, J. L., Lipson, A. L., Pupek, K. Z. & Kahvecioglu, O. Roles of Mn and Co in Ni-rich layered oxide cathodes synthesized utilizing a Taylor Vortex Reactor. *Electrochim. Acta* **391**, 138929 (2021).
114. Tan, Z. et al. Lattice engineering to alleviate microcrack of $LiNi_{0.9}Co_{0.05}Mn_{0.05}O_2$ cathode for optimization their Li^+ storage functionalities. *Electrochim. Acta* **401**, 139482 (2022).
115. Wang, Y., Zhu, Y. & Gao, P. Synthesis and characterization of Nickel-rich layered $LiNi_{1-x}Mn_xO_2$ (x=0.02,0.05) cathodes for lithium-ion batteries. *Electrochim. Acta* **427**, 140891 (2022).
116. Xi, R. et al. High-nickel and cobalt-free layered $LiNi_{0.90}Mn_{0.06}Al_{0.04}O_2$ cathode for lithium-ion batteries. *Cera. Int.* **48**, 36690-36696 (2022).

117. Zhang, S., Gao, P., Wang, Y., Li, J. & Zhu, Y. Cobalt-free concentration-gradient $Li[Ni_{0.9}Mn_{0.1}]O_2$ cathode material for lithium-ion batteries. *J. Alloys Compd*. **885**, 161005 (2021).
118. Feng, H. et al. Stabilizing $LiNi_{0.9}Mn_{0.1}O_2$ structure by Al^{3+} doping for cobalt-free lithium-ion batteries. *J. Alloys Compd.* **960**, 170676 (2023).
119. Ren, Z. et al. Improving $LiNi_{0.9}Co_{0.08}Mn_{0.02}O_2$'s cyclic stability via abating mechanical damages. *Energy Storage Mater*. **28**, 1-9 (2020).